Redox Biology 98 (2026) 104451

Contents lists available at ScienceDirect

Redox Biology

journal homepage: www.elsevier.com/locate/redox

Targeting ERO1α triggers tumor immunosurveillance in triple-negative breast cancer

Alessandro Cherubini [a,b,1], Ersilia Varone [a,1], Sara Irene Malandrin [a], Alice Marrazza [a], Giorgia Maria Renna [a,c], Serena Germani [a], Stefano Fumagalli [a], Angela Bachi [d], Angela Cattaneo [e], Michele Retini [b], Giovanni Piersanti [b], Marco Bolis [a,f], Ilaria Craparotta [a], Arianna Vallerga [a], Chiara Grasselli [a], Manuela Milani [g], Daniele Generali [g], Augusto Bleve [a,h], Ester Zito [a,b,*]

[a] Istituto di Ricerche Farmacologiche Mario Negri IRCCS, Milan, Italy
[b] Department of Biomolecular Sciences, University of Urbino Carlo Bo, Urbino, Italy
[c] Department of Molecular and Developmental Medicine, University of Siena, Siena, Italy
[d] IFOM ETS, The AIRC Institute of Molecular Oncology, Milan, Italy
[e] Cogentech SRL Benefit Corporation, Milan, 20139, Italy
[f] Bioinformatics Core Unit, Institute of Oncology Research (IOR), Bellinzona, Switzerland
[g] U.O. Patologia Mammaria e Tumori Cerebrali, Azienda Socio-Sanitaria Territoriale, Cremona, Italy
[h] IRCCS Humanitas Research Hospital, Milan, Italy

ARTICLE INFO

Keywords:
ERO1
Stress of the endoplasmic reticulum (ER stress)
UPR (unfolded protein response)
Protein N-glycosylation
Immune-check points
Triple negative breast cancer
Immunosurveillance

ABSTRACT

Triple-negative breast cancer (TNBC) remains a highly aggressive malignancy with limited responsiveness to immune checkpoint blockade. Here, we identify endoplasmic reticulum oxidoreductase 1 alpha (ERO1α; ERO1A), a key regulator of oxidative protein folding, as a determinant of tumor immunogenicity and immunotherapy response in TNBC. Unbiased proteomic profiling demonstrated that ERO1α deficiency remodels the TNBC glycoproteome, leading to enrichment of pathways associated with immune signaling. Although ERO1α loss did not affect tumor cell growth, it reshaped the immune tumor microenvironment, enhancing antigen presentation, altering myeloid-cell composition, and modulating PD-1/PD-L1–associated signaling.

Functionally, ERO1α deficiency sensitized otherwise refractory TNBC tumors to PD-1 blockade, resulting in durable tumor regression in immunocompetent hosts. In contrast, ERO1α deletion in bone marrow–derived immune cells had minimal effects on tumor growth or therapeutic response, supporting an ERO1α tumor-intrinsic mechanism. Pharmacologic inhibition of ERO1α with the novel small-molecule inhibitor I29 phenocopied ERO1α genetic deletion and enhanced the efficacy of anti–PD-1 therapy. Together, these findings identify ERO1α-dependent glycoproteome remodeling as a regulator of antitumor immunity and a therapeutically actionable mechanism of immune checkpoint responsiveness in TNBC.

1. Introduction

Triple-negative breast cancer (TNBC) accounts for 15–20% of all breast cancers and is associated with high metastatic potential, early relapse, and poor overall survival. TNBC is defined by the absence of estrogen receptor (ER), progesterone receptor (PR), and human epidermal growth factor receptor 2 (HER2) expression. This molecular profile limits the availability of targeted therapies, leaving chemotherapy and, more recently, immunotherapy as the principal treatment strategies [1]. Although immune checkpoint inhibitors targeting the PD-1/PD-L1 axis have demonstrated clinical benefit in a subset of patients, the majority of TNBC tumors remain poorly immunogenic and exhibit limited responsiveness to immunotherapy [2] [3]. Therefore, understanding the mechanisms that govern immune evasion and

This article is part of a special issue entitled: Cancer Redox & Metabolism published in Redox Biology.

* Corresponding author. Istituto di Ricerche Farmacologiche Mario Negri IRCCS Via Mario Negri 2, 20156, Milano, Italy.
E-mail address: ester.zito@marionegri.it (E. Zito).

[1] Equal contribution.

https://doi.org/10.1016/j.redox.2026.104451
Received 17 October 2026; Accepted 21 October 2026
Available online 23 October 2026
2213-2317/© 2026 Published by Elsevier B.V. This is an open access article under the CC BY-NC-ND license (http://creativecommons.org/licenses/by-nc-nd/4.0/).

identifying strategies capable of converting immune-refractory ("cold") TNBC into immune-active ("hot") tumors remain major unmet clinical needs [4].

The endoplasmic reticulum (ER) plays a central role in protein folding, redox homeostasis, and cellular stress adaptation. Perturbation of ER homeostasis induces ER stress and activates the so-called unfolded protein response (UPR), an adaptive signaling network that enables tumor cells to survive under hostile conditions, including hypoxia, oncogene activation and nutrient deprivation [5,6] [7] [8]. In addition to supporting tumor adaptation, accumulating evidence indicates that the UPR actively regulates tumor–immune interactions by promoting immune suppression [9]. The UPR mediator endoplasmic reticulum oxidoreductin 1 alpha (ERO1α; ERO1A; hereafter ERO1) is a key regulator of oxidative protein folding that, together its partner protein disulphide isomerase 1 (PDI), catalyzes disulfide bond formation in secretory and membrane proteins while also contributing to metabolic adaptation [10–12]. ERO1 expression is elevated in multiple cancer types and has been associated with poor prognosis, metastatic progression and immune evasion [13] [14] [15] [16] [17] [18]. However, the mechanisms linking ERO1 to tumor immune regulation remain incompletely understood and have not been characterized in TNBC.

In TNBC, we and others have previously demonstrated that ERO1 contributes to the oxidative folding of protumorigenic factors, including vascular endothelial growth factor (VEGF), thereby promoting angiogenesis, tumor metastases, and adaptation to hypoxic stress [19] [15] [20] [21] [22]. In addition to its pro-angiogenic activity, VEGF contributes to immune evasion by limiting T-cell recruitment and infiltration within the tumor microenvironment (TME), pointing to a potential role of ERO1 also in tumor immune regulation [23].

Consistent with previous findings, ERO1 deficiency reduces the oxidative poise of the ER, thereby enhancing MAGT1-dependent N-glycosylation of VEGF and potentially other client proteins [24–26]. Because glycosylation critically regulates not only the stability, and secretion, but also antigenicity, and immune recognition of tumor-associated proteins [27], these findings raise the possibility that lack of ERO1 may reshape the tumor glycoproteome and thereby influence tumor immunity.

Based on this foundation, we investigated whether ERO1-dependent glycoproteome remodeling influences antitumor immunity and responsiveness to PD-1 blockade in TNBC. Using integrated unbiased glycoproteomic, transcriptomic, and immunological analyses of the TME, we demonstrate that ERO1 deficiency remodels the TNBC glycoproteome, enhances myeloid-cell infiltration and antigen-presentation programs within the TME, thereby sensitizing these otherwise refractory tumors to PD-1 blockade. Furthermore, pharmacological inhibition of ERO1 phenocopies the effects of genetic ERO1 deletion in tumors and enhances antitumor immunity. Collectively, our findings identify ERO1 as a regulator of tumor–immune interactions in TNBC, linked to glycoproteome remodeling and antigen-presentation programs, and support ERO1 as a therapeutic target for combination immunotherapy.

2. Materials and methods

2.1. Analysis of ERO1 proteomics data

Proteomics data were obtained from PRIDE repository PXD024322. This dataset comprises proteomic profiles of 300 archival breast cancer specimens representing different molecular breast cancer subtypes. Tandem mass tag (TMT) peptide-spectrum match (PSM) quantification and protein annotation files, and the corresponding sample annotation tables were used for downstream analyses. For each TMT batch, reporter channels were matched to individual samples using the provided channel annotation, and samples were labeled by Study_ID and PAM50 subtype. Gene symbols were extracted from the corresponding protein annotation files. Analyses were restricted to ERO1 and the three immune checkpoint proteins CTLA-4 (CTLA4), PD-L1 (CD274), and PD-1 (PDCD1). Quantification was performed at the PSM level. Samples with low overall signal were excluded based on total reporter signal-to-noise. To correct for loading differences, total reporter abundance in each channel was scaled to a common value within each TMT plex. PSM abundances were then normalized to the corresponding pooled internal standard (PIS) channel of the same plex, and relative protein abundance was summarized from peptide-level measurements using the median of the most abundant PSMs for each protein. Protein abundance values were subsequently log2-transformed to reduce right-skewness. A sample-by-protein expression matrix was then generated after excluding pooled internal reference channels from downstream biological analyses.

Associations between ERO1 and the selected proteins were assessed using Spearman's rank correlation in the full cohort, stratified by PAM50 subtype, and separately in the TNBC subgroup. TNBC cases were defined using the study's supplementary clinical annotation as samples with a non-missing value for the TNBC Consensus Cluster variable, yielding the same number of TNBC samples reported in the original study. Scatterplots were generated with each point representing one sample annotated by Study_ID; full-cohort plots were colored by PAM50 subtype. Linear regression lines were overlaid to illustrate trends, and Spearman correlation coefficient (ρ), P value, and number of evaluable samples (n) were reported. ERO1 abundance across molecular subtypes was compared using the Kruskal-Wallis test, followed by pairwise Wilcoxon rank-sum tests with Benjamini-Hochberg correction. Normal breast tissue controls were identified from the study design annotation derived from reduction mammoplasty or annotated as normal breast tissue and compared with TNBC subset using Wilcoxon rank-sum tests. Boxplots display median, interquartile range, and 1.5 × IQR whiskers, and individual samples [28].

2.2. Breast cancer patient and tumor collection

Breast carcinoma samples were obtained at the U.O. "Patologia Mammaria e Tumori Cerebrali, Azienda Socio-Sanitaria Territoriale of Cremona, Italy" as part of routine procedures between 2005 and 2008. Human studies were conducted in accordance with approval from the local ethical committee of "Azienda Socio-Sanitaria Territoriale of Cremona" (RaLCTrVs1Ott_2000). Breast cancers were classified as Luminal A or TNBC by a pathologist using H&E staining combined with molecular profiling. Residual tissue material was used to generate a human tissue microarray (TMA), which was anonymized prior to analysis to ensure investigator blinding.

2.3. Breast cancer tissue microarray

A TMA comprising 52 TNBC cases and 48 Luminal A cases was generated using a computer-assisted tissue microarrayer (Model TMA Galileo CK4500, Integrated Systems Engineering srl, Milano, Italy). Tissue cores of either 1.0 mm or 0.6 mm in diameter were extracted from FFPE blocks from areas on consecutive H&E-stained sections.

2.4. PD-1 and PD-L1 expression analysis in breast cancer tissues

Five-μm-thick tumor sections were incubated at 70°C for 40 min, then deparaffinized in xylene and rehydrated through graded ethanol solutions (100%, 95%, 85%, and 75%). Antigen retrieval was performed by heating the sections in citrate buffer (pH 6; Biocare Medical, CB910 M) using a microwave oven for 15 min.

Slides were treated with 1% H_2O_2 for 10 min at room temperature (RT), followed by three washes in 0.01 M PBS for 5 min each. Non-specific binding was blocked using 10% normal goat serum (NGS) and 0.3% Triton X-100 in PBS for 1 h. Sections were incubated overnight at 4°C with monoclonal PD-L1 (E1L3N, 13684 Cell Signaling Technology) or PD-1 (NAT105, ab52587 abcam) antibody diluted 1:100 in PBS containing 1% NGS. After washing, sections were incubated with a biotinylated secondary antibody (1:200 in PBS containing 1% NGS) for

1 h at RT. Following additional washes in PBS and TNT buffer (0.04% Tween-20 in 0.1 M TBS), slides were incubated with a blocking reagent (AKOYA Biosciences, NEL701A001KT) for 1 h and 30 min at RT. Sections were then incubated with streptavidin-HRP (1:100) in blocking reagent for 30 min at RT. Signal amplification was achieved by incubation with fluorescein (1:300) in amplification diluent (AKOYA Biosciences, NEL701A001KT) for 8 min at RT. Nuclear counterstaining was performed using Hoechst (H5369, Termofisher) (1 μg/mL) for 10 min. After final washes in PBS and sterile water, sections were mounted using ProLong Gold antifade reagent. Images were acquired using a Nikon A1 confocal microscope with a 20× objective, employing large area scanning and avoiding signal saturation. PD-1 and PD-L1 fluorescence intensity was quantified across the entire tissue section and expressed as mean grey pixel intensity. Digital image analysis was performed using custom-developed ImageJ algorithms. Correlation analysis between ERO1, whose values were reported in Ref. [29], and PD-1 or PD-L1 expression was performed using ERRE software package.

2.5. E0771 and MDA-MB-231 breast cancer cell line

The murine E0771 breast cancer cell line (940001-A, CH3 BioSystems) was cultured under standard conditions and used within two weeks of thawing [30]. Cells were routinely tested and confirmed to be free of Mycoplasma contamination.

For gene editing, E0771 cells were transfected with CRISPR/Cas9 plasmids targeting ERO1α (Santa Cruz Biotechnology, Cat. No. sc-424456), containing three gene-specific guide RNAs (gRNAs), according to the manufacturer's instructions. ERO1-knockout (KO) clones were identified by Sanger sequencing to verify the presence of indels and were further validated by Western blotting for ERO1 before expansion for downstream experiments. Human ERO1KO MDA-MB-231 cells were generated as described in Ref. [19].

2.6. Hypoxic chamber

E0771 and MDA-MB-231 cells were transferred to hypoxic chamber (Ruskinn Invivo2 400, UK) at 37°C for 20 h and maintained in deoxygenated culture medium at the following gas concentrations: O_2 0.1%, CO_2 5%. Control cells were maintained in standard culture medium in a normoxic incubator.

3. MTS

For proliferation assays, 6000 cells per well were seeded in 96-well plates and cultured in complete medium supplemented with 10% fetal bovine serum (FBS). Cell viability was assessed using the MTS assay. Following incubation, cells were treated with MTS reagent [3-(4,5-dimethylthiazol-2-yl)-5-(3-carboxymethoxyphenyl)-2-(4-sulfophenyl)-2H-tetrazolium] in combination with phenazine methosulfate (PMS), according to the CellTiter 96® Aqueous Non-Radioactive Cell Proliferation Assay (Promega) protocol. Absorbance was measured using a TECAN Infinite M200 plate reader at 490 nm.

3.1. Motility assays

Cell motility was assessed using modified Boyden chambers fitted with gelatin-coated polycarbonate Nucleopore filters (8-μm pore size). For HUVEC migration assays, conditioned medium collected from equal numbers of WT and ERO1 KO E0771 cells was used as a chemoattractant in the lower chamber. The anti-VEGF antibody B20.4.1.1 (B20; 250 ng/μL; Genentech, South San Francisco, CA, USA) was added to the conditioned medium and maintained throughout the assay. HUVECs were resuspended in DMEM containing 0.1% BSA at a concentration of 0.75×10^6 cells/mL and seeded into the upper chamber. Migration assays were performed at 37°C in a humidified atmosphere containing 5% CO_2 for 6 h. To evaluate E0771 cell migration, WT and ERO1 KO E0771 cells were seeded in the upper chamber, while conditioned medium from NIH3T3 fibroblasts was used as the chemoattractant in the lower chamber. Cells were resuspended in high-glucose DMEM supplemented with 0.1% BSA at a concentration of 1×10^6 cells/mL. Assays were performed at 37°C in a humidified 5% CO_2 atmosphere for 6 h. At the end of the incubation period, filters were fixed and stained using Diff-Quik (Marz-Dade, Düdingen, Switzerland). Non-migrated cells on the upper surface of the membrane were removed, and cells that had migrated to the lower surface were counted in ten randomly selected high-power fields per filter under light microscopy. Results were expressed as the mean number of migrated cells per field as in Ref. [19].

3.2. Glycosylated protein enrichment from E0771 cells

WT and ERO1 KO E0771 were cultured under normoxic or hypoxic conditions. Following treatment, WT and ERO1 KO E0771 cells were washed, scraped, and lysed in RIPA buffer (without EDTA or sodium deoxycholate) supplemented with EDTA-free protease inhibitors. Total protein concentration was determined using a BCA protein assay. Glycosylated proteins were enriched using the Pierce Glycoprotein Isolation Kit by lectin-based affinity purification with wheat germ agglutinin (WGA) (Thermo Scientific™, Cat. No. 89805) or concanavalin A (Con A) (Thermo Scientific™, Cat. No. 89804), according to the manufacturer's instructions. Following elution from WGA or ConA columns, buffer exchange was performed using Amicon Ultra-0.5 centrifugal filter units (3 kDa MWCO; Merck Millipore, Cat. No. UFC5003). Samples were washed four times with phosphate-buffered saline (PBS) containing EDTA-free protease inhibitors to ensure compatibility with downstream analyses.

3.3. Sample preparation for proteomics

ConA lectin-enriched proteins (three biological replicates per condition) and WGA-enriched proteins (one sample per condition) from secreted and intracellular fractions, as well as the corresponding input samples from hypoxia-treated WT and ERO1 KO E0771 cells, were processed for proteomic analysis. Protein extracts were solubilized in 8 M urea and 100 mM Tris-HCl, pH 8.0 (UA buffer), and protein concentration was determined using a BCA assay.

3.4. Protein digestion and peptide purification

10 μg of protein samples in UA buffer were subjected to in-solution digestion using the filter-aided sample preparation workflow. Cysteine residues were reduced and alkylated with 10 mM tris(2-carboxyethyl) phosphine (TCEP) and 40 mM 2-chloroacetamide (CAM), respectively. Proteins were then deglycosylated with PNGase F and digested sequentially with Lys-C and trypsin overnight. Peptides were desalted using C18 StageTips [31] prior to mass spectrometric analysis.

3.5. nLC and mass spectrometry

LC–MS/MS analysis was performed on a nanoLC system (Vanquish Neo, Thermo Fisher Scientific) coupled to an Orbitrap Exploris 480 mass spectrometer equipped with a FAIMS Pro interface (Thermo Fisher Scientific) operating at CVs −50/-70V. Peptides were separated using a 25 cm × 75 μm ID nanoLC column packed in-house with ReproSil-Pur C18-AQ 1.9 μm beads (Dr. Maisch GmbH, Germany). Peptide separation was performed at a flow rate of 200 nL/min using a 45 min gradient, increasing solvent B from 0% to 5% in 3 min (solvent A: 0.1% formic acid in water; solvent B: 0.1% formic acid in 80% acetonitrile). The gradient consisted of 50% solvent B in 30 min and 60% solvent B in 5 min, followed by a wash step at 100% solvent B for 7 min. Data were acquired in positive data-independent acquisition (DIA) mode with the following ion source parameters: Spray Voltage 2200 V, funnel RF lens at 40%, Ion Transfer Tube Temp 300°C and total carrier gas flow 3,7 L/

min. Full MS spectra (400-1000 Th) were acquired at a Resolution of 120 K, with a Normalized AGC Target of 300%, a maximun IT of 55 ms and Microscan 1. Precursors selected for DIA scan should have a charge state of 2. MS/MS spectra were acquired at a Resolution of 30 K, with a Normalized AGC Target of 1000%, maximum IT set to Auto, Microscan 1, HCD Normalized Collision Energy of 32%, and an Isolation Window of 3 *m/z*.

3.6. Data processing and analysis

Secretome and intracellular samples were processed separately. Raw DIA data were analyzed using Spectronaut (v18.5, Biognosys) employing the direct DIA + search workflow, iRT-based retention time regression, and the UniProt CP_Mouse database. Trypsin/P was specified as the digestion enzyme, allowing up to two missed cleavages. Carbamidomethylation of cysteine was set as a fixed modification, while asparagine deamidation, methionine oxidation and protein N-terminal acetylation were set as variable modifications; PTM localization filter was turned on with the localization probability cut-off of 0.75. Peptide and protein FDRs were at 1% and Method Evaluation was enabled. Quantification was performed based on MS2 peptide peak areas. The exported reports were subjected to Label-Free quantitative statistical analysis using Perseus (ver. 2.0.10.0) [32]. Normalization width-adjustment and supervised Hierarchical Clustering analysis were performed to generate Heatmaps comparing WT and ERO1A KO samples. Statistical significance was assessed using *t*-test with a p-value thresholds of 0.05. Pathway enrichment analysis was performed using Enrichr [33]. Gene names corresponding to statistically significant proteins (Sig+) identified between WT and ERO1 KO samples were used as input for both intracellular and secretome datasets. Reactome pathway enrichment results were filtered using a significance threshold of $p < 0.05$.

3.7. Biochemical analyses of lectin-enriched samples

For biochemical validation, equal amounts of lectin-enriched glycoproteins were resolved by SDS–PAGE followed by Coomassie staining and Western blot analysis. Membranes from E0771 cells were incubated with mouse anti–PD-L1 primary antibody (Abcam, Cat. No. 213480) and membranes from MDAMB231 cells were incubated with human anti–PD-L1 primary antibody (Abcam, Cat. No.205921), followed by incubation with appropriate horseradish peroxidase (HRP)-conjugated secondary antibodies and chemiluminescent detection. To assess the glycosylation status of PD-L1, E0771 cell lysates obtained under normoxic and hypoxic conditions were treated with PNGase F (New England Biolabs, Cat. No. P0704S) or Endo H (New England Biolabs, Cat. No. P0702S), according to the manufacturer's instructions, prior to SDS–PAGE and Western blot analysis.

3.8. Ro-GFP2 assessment of ER redox

To monitor ER redox poise and assess differences among wild-type (WT) and ERO1-KO HeLa cells, with or without treatment with 55 μM β-mercaptoethanol (β-ME) added to the culture medium for 48 h, we used the ER-localized ratiometric redox sensor roGFP2, as described in Ref. [34].

3.9. Mice

Seven-week-old mice C57/BL6J-Ptprcem6Lutzy/J (JAX:033076) and C57/BL6J mice were obtained from Charles River Laboratories (Calco, Italy) and maintained under specific-pathogen-free conditions. For bone marrow cell isolation, WT and ERO1-KO mice were obtained from internal breeding colonies [35]. All animal studies were reported in accordance with the ARRIVE guidelines and were conducted in compliance with applicable laws, regulations, and institutional policies governing the care and use of laboratory animals, including Italian Legislative Decree No. 26/2014; authorization 19/2008-A issued by the Italian Ministry of Health on March 6, 2008; and experimental authorizations 896/2023-PR and 28/2025-PR issued to E. Zito. Experiments were also conducted in accordance with the institutional regulations and policies of the Mario Negri Institute, including personnel authorization procedures and the Quality Management System Certificate (UNI EN ISO 9001:2008; registration no. 6121), as well as European Union Directive 2010/63/EU on the protection of animals used for scientific purposes. All procedures were performed in accordance with the Guidelines for the Welfare and Use of Animals in Cancer Research [36].

3.10. Bone marrow transplantation

Bone marrow transplantation experiments were performed using female WT and ERO1 KO donor mice less than 12 weeks of age.

Prior to transplantation, recipient mice underwent to myeloablative total-body irradiation using a split-dose regimen consisting of 4.5 Gy followed by an additional 4.5 Gy administered 2 h later (total dose: 9 Gy) using an XRADGIL irradiator (Gilardoni). Following irradiation, mice were maintained under standard housing conditions with free access to food and water.

Bone marrow cells were isolated under sterile conditions from both femurs and tibias of donor mice. Briefly, bones were excised, cleaned of surrounding soft tissue, and flushed with sterile phosphate-buffered saline (PBS). Bone marrow cell suspensions were passed through a 70-μm cell strainer to obtain a single-cell suspension. Cells were collected by centrifugation, resuspended in sterile PBS, and counted using a hemocytometer or automated cell counter.

Six hours after irradiation, recipient mice were anesthetized and transplanted with donor bone marrow cells. A total of 5×10^6 bone marrow cells suspended in sterile PBS was administered to each recipient by retro-orbital intravenous injection. Ten to twelve mice for condition were transplanted. Recipient mice were monitored regularly following transplantation and allowed to undergo hematopoietic reconstitution before subsequent experimental procedures.

3.11. Assessment of bone marrow reconstitution by flow cytometry

To evaluate donor-derived hematopoietic reconstitution, peripheral blood was collected from recipient CD45.1 mice two weeks after bone marrow transplantation with bone marrow cells isolated from CD45.2 WT or ERO1 KO donor mice. Following red blood cell lysis, leukocytes were stained with fluorochrome-conjugated antibodies against CD45.1 (APC-Cy7, clone A20, BioLegend) and CD45.2 (BV650, clone 104, BioLegend) and analyzed by flow cytometry. Donor-derived hematopoietic reconstitution was assessed by determining the percentage of CD45.2-positive cells within the circulating cell population.

3.12. Breast tumor models and treatments

Two weeks after bone marrow transplantation, WT and ERO1 KO E0771 cells (1×10^6 cells per mouse) were orthotopically injected into the mammary fat pad of female C57BL/6 J mice. Once tumors became palpable (typically 5 days after tumor cell inoculation), mice were randomized to receive either 200 μg of anti-PD-1 antibody (ICH1132, clone RMP1-14) or an isotype control antibody (ICH2244, anti-trinitrophenol) by intraperitoneal (i.p.) injection every 3 days for a total of three administrations, as previously described [37].

For combination therapy experiments, mice received either the ERO1 inhibitor I29 or vehicle control (Cremophor EL and PEG400). I29 treatment was initiated 2 day before the first anti-PD-1 administration and was delivered by intraperitoneal injection at a dose of 10 mg/kg every 2 days for 22 days (11 injections in total), as previously described [38] [29]. Investigators were not blinded to treatment allocation. Tumor growth was monitored using a Vernier caliper, and tumor volume was calculated according to formula $D \times d^2/2$, where D represents the largest

tumor diameter and d the smallest diameter. Body weight and overall health status were monitored daily throughout the study. Twenty-five days after tumor cell inoculation, mice were euthanized and primary tumors were harvested. Tumor samples were randomly selected for downstream analyses.

3.13. Flow cytometry analysis of orthotopic breast tumors

Primary tumors derived from E0771 cells were excised and mechanically minced into small fragments. Tumor tissues were enzymatically digested in DMEM containing 0.5 mg/mL collagenase IV (Sigma) and 40 μg/mL DNase I for 30 min at 37°C. The resulting cell suspensions were filtered through a 70-μm cell strainer to obtain single-cell suspensions. Red blood cells were removed using ACK lysis buffer for 5 min at room temperature. Cells were then washed and resuspended in PBS supplemented with 5% FBS. Cells were stained for 20 min at 4°C with fluorochrome-conjugated antibodies (BioLegend unless otherwise indicated) in appropriate panels. A viability dye (LIVE/DEAD™ Fixable Near-IR, Invitrogen) was used to exclude dead cells. Samples were acquired on a CytoFLEX LX flow cytometer (Beckman Coulter) using CytExpert software and analyzed with Kaluza 2.0 software. Doublets and debris were excluded using forward scatter (FSC) and side scatter (SSC) gating strategies. $CD45^+$ leukocytes were first identified, and myeloid and lymphoid populations were subsequently defined. Myeloid-derived suppressor cells (MDSCs) were identified as CD11b + Ly6G + $Ly6C^{low}$ as neutrophile granulocytic MDSCs (PMN-MDSCs or neutrophile cells) and CD11b + Ly6G–$Ly6C^{high}$ monocytic MDSCs (M-MDSCs or monocytic cells). Macrophages or Tumor-associated macrophages (TAMs) were defined as CD11b + $Ly6C^{low}$/–F4/80+ cells and CD11b + CD11c + as dendritic cells. T lymphocytes were gated as $CD3^+$ cells and further subdivided into $CD4^+$ (helper) and $CD8^+$ (cytotoxic) subsets. PD-1 expression was analyzed in $CD4^+$ and $CD8^+$ T cells, whereas PD-L1 expression was assessed in myeloid populations, including MDSCs and TAMs. Additional lymphoid populations were analyzed using a dedicated panel including $CD19^+$ B cells, NK1.1+ NK cells, regulatory T cells (CD4+FoxP3+), and granzyme B expression in cytotoxic lymphocytes.

Two complementary antibody panels were used:

Myeloid/tumor-associated compartment.

Marker	Fluorochrome	Clone	Company	Catalog
Live/Dead	IR876	-	Invitrogen	L34981
CD31	AF488	MEC13.3	BioLegend	102513
CD45.1	APC-Cy7	A20	BioLegend	110716
CD45.2	BV650	104	BioLegend	109836
CD11b	PerCP-Cy5.5	M1/70	BioLegend	101227
CD11c	BV605	N418	BioLegend	117333
Ly6C	BV421	HK1.4	BioLegend	128031
Ly6G	AF700	1A8	BioLegend	127621
F4/80	PE-Cy7	BM8	BioLegend	123113
PD-L1	APC	10F.9G2	BioLegend	124311
MHC-I	PE	AF6-88.5	BioLegend	116507

Lymphoid cell compartment.

Marker	Fluorochrome	Clone	Company	Catalog
Live/Dead	IR876	-	Invitrogen	L34981
CD45.1	APC-Cy7	A20	BioLegend	110716
CD45.2	BV650	104	BioLegend	109836
CD11b	PerCP-Cy5.5	M1/70	BioLegend	101227
CD19	PE/Dazzle 594	6D5	BioLegend	115553
NK1.1	PE-Cy7	PK136	BioLegend	108713
CD3	BV605	145-2C11	BioLegend	100351
CD4	AF700	GK1.5	BioLegend	100429
CD8	BV785	53-6.7	BioLegend	100749
PD-1	APC	29F.1A12	BioLegend	135209
CTLA-4	BV421	UC10-4B9	BioLegend	106311
FoxP3	PE	FJK-16s	eBioscience	12-5773-80
Granzyme B	FITC	NGZB	eBioscience	11-8898-80

3.14. PD-1 and PD-L1 immunofluorescence on tumor sections

Frozen tissue blocks were sectioned at a thickness of 10 μm using a cryostat. For immunofluorescence staining, sections were first equilibrated by transferring the slides from −20°C to +4°C for 20 min, followed by an additional 20 min at room temperature (RT). The sections were then fixed in 4% paraformaldehyde (PFA) in PBS for 10 min at RT. To quench endogenous peroxidase activity, slides were incubated in 1% hydrogen peroxide (H_2O_2) in PBS for 10 min at RT. After three washes in PBS, non-specific binding sites were blocked for 1 h at RT using a blocking solution containing 10% normal goat serum (NGS) and 0.3% Triton X-100 in PBS. Sections were then incubated overnight at +4°C with either anti-PD-1 antibody ([EPR20665], ab214421, Abcam) or anti-PD-L1 antibody ([EPR20529], ab213480, Abcam), both diluted 1:100 in PBS containing 1% NGS. After three washes in PBS, sections were incubated for 1 h at RT with a goat anti-rabbit biotinylated secondary antibody diluted 1:200 in PBS containing 1% NGS. Signal amplification was performed using a tyramide signal amplification (TSA) Fluorescein System (NEL701A001KT, Akoya Biosciences). Briefly, sections were washed with TNT buffer (0.1 M Tris-buffered saline, pH 7.6, 0.04% Tween-20) and incubated in TNB blocking buffer (0.1 M Tris-buffered saline, pH 7.6, 0.5% blocking reagent) for 1.5 h at RT. Slides were then incubated with streptavidin-HRP (1:100 in TNB) for 30 min at RT. After additional washes in TNT buffer, the fluorescent signal was developed by incubating the sections with fluorescein tyramide reagent (1:300 in amplification diluent) for 8 min at RT. Nuclei were counterstained with Hoechst (1 μg/mL in PBS) for 10 min at RT. Finally, slides were washed in distilled water and mounted with ProLong Gold Antifade Mountant.

3.15. Magnetic resonance imaging (MRI)

MRI of tumors from euthanized mice were performed on a Bruker BioSpec 70/30 system equipped with Bruker NEO electronics (Bruker, Ettlingen, Germany). Two actively decoupled radiofrequency coils were used: a volume coil (8.6 cm diameter) for transmission and a 2 × 2 array surface coil for signal reception.

A rapid 2D RARE (rapid acquisition with relaxation enhancement) T2-weighted sequence was acquired to assess tumor size and morphology. Images were obtained with a voxel size of $0.118 \times 0.118\ mm^2$ (matrix = 212 × 212; field of view = $25 \times 25\ mm^2$) and a slice thickness of 0.7 mm. Acquisition parameters were as follows: repetition time (TR) = 5000 ms, effective echo time (TEeff) = 50 ms, RARE factor = 16, and 4 signal averages.

3.16. RNA sequencing analysis from breast tumors

RNA was extracted from 4 WT and ERO1 KO E0771 tumors in mice with WT or ERO1 KO bone marrow using the Qiagen RNeasy kit (16 tumors in total). RNA concentration was measured with the Qubit™ RNA Broad Range Assay Kit (Invitrogen, Waltham, MA, USA), and RNA quality was assessed using the 4200 TapeStation system (Agilent Technologies, Santa Clara, CA, USA). Libraries were prepared using the TruSeq Stranded Total RNA Library Prep kit (Illumina, San Diego, CA, USA). RNA sequencing was performed on an Illumina NextSeq 500 platform. The overall quality of sequencing reads was assessed using FastQC (v0.11.9). Sequence alignment of stranded total RNA reads to the mouse reference genome (GRCm39) was performed using STAR (v.2.7.11b) in two-pass mode. Gene expression was quantified at the gene level using the GENCODE mouse annotation (GRCm39, M38 release GTF file). Raw counts were normalized using the variance stabilizing transformation (VST) implemented in the R statistical environment. Differential gene expression analysis was performed using STAR (v.1.48.2).

3.17. Pathway analysis and network visualization

Gene set enrichment analysis (GSEA) was repeated using the clusterProfiler R package (v4.16.0), implementing the fgsea algorithm. For this analysis, mouse-specific gene-set collections from the Molecular Signatures Database (MSigDB) were used directly in gmt format. Specifically, the following MSigDB mouse collections were included: MH Hallmark gene sets, M2 Curated gene sets, M7 Immunologic signature gene sets, and M8 Cell type signature gene sets. Genes were pre-ranked based on a signed significance metric defined as $-\log10(\text{p-value}) \times \text{sign}$ (log2 fold change), where p-values and log2 fold changes were derived from the DESeq2 analysis. For each gene set, normalized enrichment scores (NES), nominal p-values, and FDR-adjusted q-values were computed. Gene sets with FDR q-value < 0.05 were considered significantly enriched. GSEA results were visualized as enrichment networks using Cytoscape (v3.10.1) with the Enrichment Map app. Enrichment maps were generated using a node significance threshold of q-value $\leq$ 0.10 and an edge similarity cutoff of 0.375. In the resulting networks, each node represents a gene set enriched in at least one contrast. Node size is proportional to the number of genes in the gene set. Nodes are displayed as pie charts summarizing enrichment across contrasts, with each slice corresponding to a specific comparison. Slice color encodes the normalized enrichment score (NES), with positive values shown in red, negative values in blue, and non-significant enrichments in grey. Edges represent gene overlaps between gene sets, with edge thickness and color intensity proportional to the degree of overlap. Pathways of interest were subsequently identified and grouped into broader functional categories through manual curation based on gene set composition and biological annotation. A heatmap was generated representing the gene annotated for the selected pathway of interest REACTOME_CO_INHIBITION_BY_PD_1. To provide a broader overview of the most enriched biological programs, GSEA was subsequently recalculated using an expanded custom GMT file that also included the MSigDB mouse M5 Ontology gene sets. The top 10 positively enriched gene sets for the indicated comparison were selected based on FDR-adjusted q-value and NES ranking and visualized as bar plots. For immune-focused network visualization, GSEA results were filtered to retain only MSigDB mouse M7 Immunologic signature gene sets. This immune-focused network was generated using only the indicated comparison DESeq2 contrast. These results were visualized as enrichment networks using Cytoscape (v3.10.1) with the EnrichmentMap app, using the same node significance and edge similarity thresholds described above. For the immune-focused enrichment network, heatmaps were generated for all pathways represented in the network. For each pathway, the top 50 genes were selected based on the absolute log2 fold change and visualized using gene-level log2 fold change values from the DESeq2 analysis. Genes with an adjusted p-value < 0.05 were marked with an asterisk in the heatmaps.

3.18. Single-cell RNA sequencing

Three tumors from each experimental group (WT tumor/WT bone marrow, ERO1 KO tumor/WT bone marrow, WT tumor/ERO1 KO bone marrow, and ERO1 KO tumor/ERO1 KO bone marrow) were processed for single-cell RNA sequencing (12 tumors in total). Following the manufacturer's instructions for the Chromium GEM-X Single Cell 3′ v4 kit (10x Genomics), single-cell suspensions were counted and loaded onto the Chromium X platform (10x Genomics) to capture approximately 18,000–20,000 cells per sample. cDNA synthesis, amplification, and library preparation were then performed according to the manufacturer's protocol. Library quality and quantity were assessed using the 4200 TapeStation (Agilent Technologies) and Qubit Fluorometer (Thermo Fisher Scientific), respectively. Libraries were pooled into two sets of six samples and sequenced in two independent runs on an Illumina NextSeq 2000 using the read configuration recommended by 10x Genomics.

Single-cell RNA-seq data were analyzed using Seurat v5 [39]. Count matrices generated by Cell Ranger were imported from the filtered feature-barcode matrices, and each sample was processed as an independent Seurat object before merging. Cells were filtered according to standard quality-control metrics, including the number of detected genes, total UMI counts and mitochondrial read fraction. Cells with high mitochondrial content, low gene or UMI counts, or excessively high UMI counts were excluded. Doublets were identified independently within each sample using scDblFinder [40], and only singlet cells were retained for downstream analysis. After quality control and doublet removal, counts were log-normalized, highly variable genes were identified using the variance-stabilizing transformation method, and cell-cycle scores were calculated using mouse-matched S and G2/M gene sets. S and G2/M scores were regressed out during data scaling before principal component analysis. Principal component analysis was performed, and sample-level batch effects were corrected using Harmony integration [41] through the Seurat v5 Integrate Layers workflow. UMAP embeddings and graph-based clustering were computed from the Harmony-corrected latent space.

All analyses were performed separately according to bone marrow genotype. In the WT bm setting, tumors derived from WT and ERO1 KO cells were compared after exclusion of one low-quality ERO1 KO tumor. In the ERO1 KO bm setting, WT and ERO1 KO tumors were compared in the ERO1-deficient bone marrow background. The immune compartment was subset from each bone marrow-specific object and re-analyzed independently by repeating normalization, variable feature selection, scaling, PCA, Harmony integration, UMAP dimensionality reduction and clustering.

Immune-cell identities were assigned using SingleR with the ImmGen reference dataset [42]. Main ImmGen labels were used to define broad immune populations for visualization and downstream composition analyses. T-cell subsets populations, including Treg-like and CD4-positive populations, were retained within the broader T-cell compartment when they were not resolved as separate main ImmGen labels. Immune composition was quantified at the biological replicate level. For each sample, the number of cells assigned to each immune population was divided by the total number of immune cells in the same sample and multiplied by 100. Summary plots show the mean percentage across biological replicates, with error bars representing the standard error of the mean. Statistical comparisons between WT and ERO1 KO tumors were first performed independently within each bone marrow genotype. To assess the overall effect of tumor cell–intrinsic ERO1 deficiency, data from mice reconstituted with WT and ERO1 KO bone marrow were subsequently pooled according to tumor genotype, and WT and ERO1 KO tumors were compared for each immune cell population.

4. Statistics

Statistical analyses were performed using GraphPad Prism (GraphPad Software, San Diego, CA, USA). The specific statistical tests and sample sizes (N) are indicated in the corresponding figure legends. Prior to analysis, data distribution was assessed for normality.

Comparisons between two independent groups with normally distributed data were performed using an unpaired, two-tailed Student's *t*-test. For experiments involving more than two groups or multiple variables, one-way or two-way analysis of variance (ANOVA) was conducted, followed by Sidak's multiple-comparisons post hoc test.

For *in vivo* experiments, the minimum number of animals required per group was determined by an a priori power analysis using G*Power software, based on the expected effect size, significance level, and statistical power.

Data are presented as mean ± standard error of the mean (SEM) or mean ± standard deviation (SD), as indicated in the figure legends. A P value < 0.05 was considered statistically significant. Statistical significance is indicated as follows: $P < 0.05$ (*), $P < 0.01$ (**) and $P < 0.001$ (***).

Protein abundance values were first normalized for loading differences and then normalized to the pooled internal standard (PIS) within each TMT plex. Normalized protein abundance values were subsequently log2-transformed before analysis to reduce positive skewness, improve homoscedasticity across the measurement range and convert multiplicative differences into an additive scale. Because protein abundance distributions were not assumed to be Gaussian and subgroup sizes were unequal, non-parametric statistical methods were used throughout. Spearman's rank correlation coefficient was selected because it does not rely on normality assumptions and is appropriate for quantifying relationships between continuous variables. Correlation analyses were performed using complete cases only; therefore, the number of evaluable samples varied across comparisons. The Kruskal-Wallis test is a non-parametric method suitable for comparing more than two independent groups. When overall differences were detected, pairwise comparisons were performed using the Wilcoxon rank-sum test. To account for multiple testing in pairwise subtype comparisons, P values were adjusted using the Benjamini-Hochberg false discovery rate (FDR) correction. Raw gene-level count data were analyzed in DESeq2 using its negative binomial generalized linear model framework for differential expression testing. Count normalization was performed internally by DESeq2 for model fitting, whereas the variance stabilizing transformation (VST) was applied only for downstream visualization and exploratory analyses. Differential expression results were reported as log2 fold changes and associated P values, and multiple testing correction was performed using the Benjamini-Hochberg false discovery rate (FDR) method. Genes with adjusted P values below the 0,05 threshold were considered differentially expressed. For pathway-level analyses, genes were ranked using a signed significance metric defined as $-\log10$(P-value) $\times$ sign (log2 fold change), thereby integrating both the strength and direction of differential expression into a single score. GSEA was performed using the fgsea algorithm as implemented in cluster Profiler, and pathway significance was assessed using NES, nominal P-values, and FDR-adjusted q-values. Gene sets with FDR $q < 0.05$ were considered significantly enriched. For enrichment network visualization in Cytoscape/Enrichment Map, significance and similarity thresholds were applied for display purposes rather than for additional statistical inference. Specifically, networks were generated using a node significance threshold of $q \leq 0.10$ and an edge similarity cutoff of 0.375. For heatmap visualization of selected pathways, genes were ranked by the absolute value of the log2 fold change, and genes with adjusted P values < 0.05 were specifically annotated. Unless otherwise specified, all statistical tests were two-sided.

5. Results

5.1. ERO1 protein expression is upregulated in TNBC and shows limited association with immune checkpoint expression

We previously analyzed ERO1 mRNA expression in breast cancer and matched normal breast tissues from The Cancer Genome Atlas (TCGA) and reported higher ERO1 expression in the more aggressive basal-like breast cancer subtype, including TNBC [19] [13].

To determine whether ERO1 protein abundance also differs among breast cancer subtypes, we analyzed proteomic data from the PXD024322 dataset comprising 300 archival FFPE breast cancer specimens representing the four PAM50 subtypes, together with normal breast tissue samples. After PSM-level quantification, loading normalization, and normalization to the pooled internal standard (PIS), ERO1 protein levels varied significantly across PAM50 subtypes (Kruskal–Wallis test, $P = 6.34 \times 10^{-34}$). Pairwise Wilcoxon tests revealed that all tumor PAM50 subtypes displayed significantly higher ERO1 abundance than normal breast tissue. ERO1 was preferentially enriched in more aggressive tumors, such as the HER2-enriched and basal-like subtypes. Consistent with this pattern, ERO1 protein levels were also significantly increased in TNBC compared with normal breast tissue ($P = 7.17 \times 10^{-18}$) (Fig. 1A).

We next investigated whether ERO1 protein abundance was associated with the expression of the immune checkpoint proteins PD-L1, PD-1 and CTLA-4. Correlation analyses revealed no significant association between ERO1 and PD-1 or CTLA-4 in the overall cohort, and no significant association with any of these immune checkpoint proteins within individual PAM50 subtypes or within the TNBC subgroup (Fig. 1B). In contrast, a weak positive correlation between ERO1 and PD-L1 was observed in the full cohort analysis (Fig. 1B).

To experimentally evaluate the relationship between ERO1 and immune checkpoint expression in breast cancer, we analyzed a tissue microarray (TMA) comprising 100 human breast tumor samples previously classified as either Luminal A or TNBC. PD-1 and PD-L1 expression levels were assessed by immunofluorescence staining. In contrast to ERO1, whose expression was significantly elevated in TNBC as previously reported, neither PD-1 nor PD-L1 expression differed significantly between Luminal A and TNBC tumors; however, distinct staining patterns were observed between the two subtypes (Fig. 1C and Supplementary Fig. 1) [29]. Correlation analysis revealed a weak positive correlation between ERO1 and PD-L1 expression ($P = 0.005$), whereas no significant correlation was observed between ERO1 and PD-1 expression (Fig. 1D). Collectively, these findings indicate that ERO1 expression is enriched in TNBC but shows limited association with baseline immune checkpoint expression, suggesting that ERO1 may regulate tumor–immune interactions through other mechanisms [19].

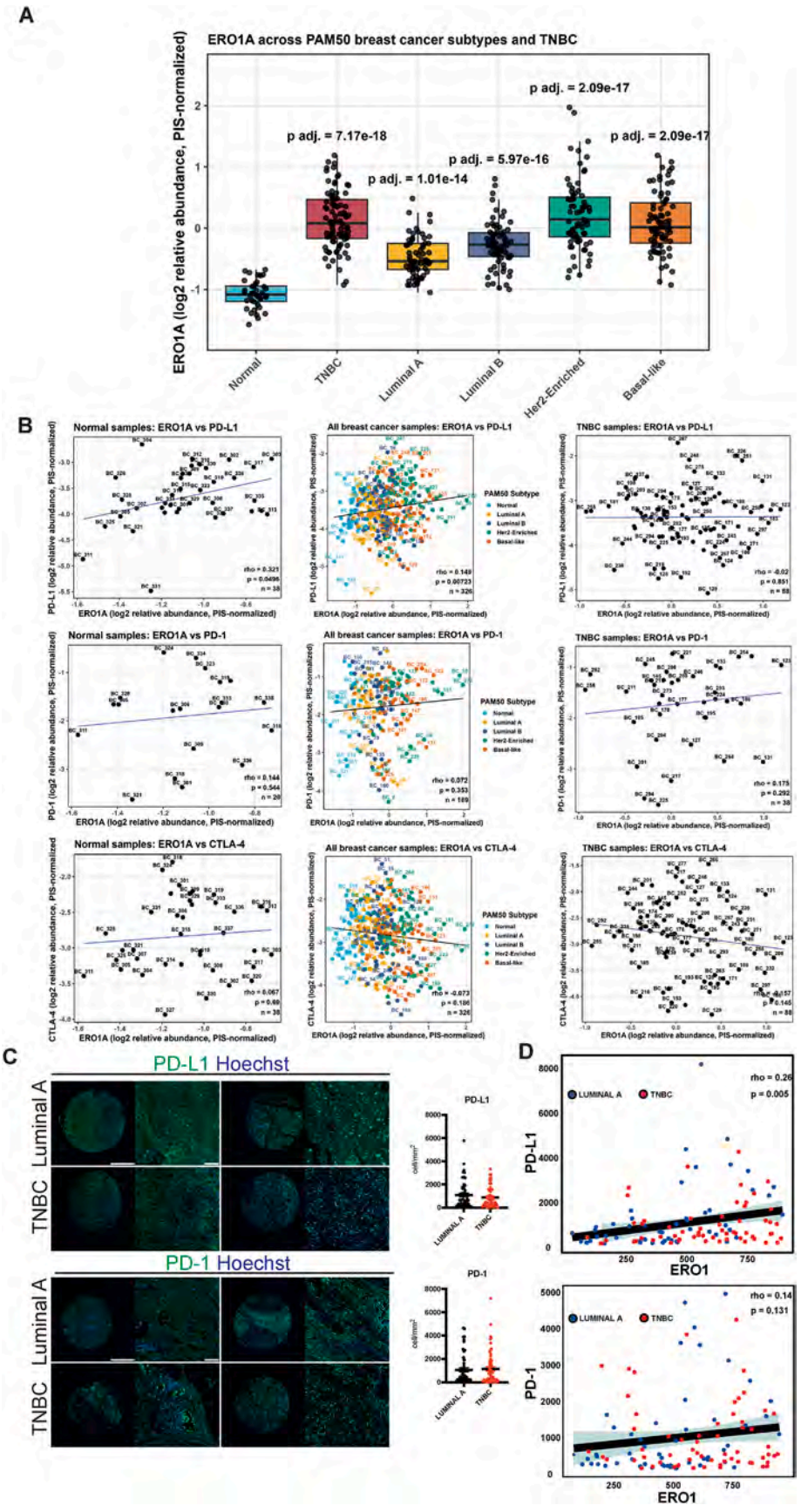
5.2. Immune system pathways are enriched in the secreted glycoproteome from ERO1 KO E0771 TNBC cells

To investigate whether ERO1 influences tumor cell growth and immune regulation in murine E0771 TNBC cells [30], we generated ERO1 knockout (KO) clones using CRISPR/Cas9 technology. Multiple independent ERO1 KO clones were obtained and validated (Fig. 2A).

Cell proliferation was assessed using an MTS assay, whereas migration assays were performed to evaluate both the migratory capacity of E0771 cells and their ability to act as a chemoattractant for human umbilical vein endothelial cells (HUVECs). Loss of ERO1 did not significantly affect the growth kinetics of E0771 cells under either normoxic or hypoxic conditions (Fig. 2B) or their migratory capacity (Fig. 2C). However, ERO1 deficiency significantly reduced the ability of E0771-conditioned medium to promote HUVEC migration (Fig. 2D). These results indicate that ERO1 ablation does not affect the intrinsic proliferative or migratory properties of E0771 cells but impairs their capacity to stimulate endothelial cell migration.

Protein glycosylation is a hallmark of cancer cells and plays important roles in immune surveillance and tumor–immune interactions [43]. Because we previously demonstrated that ERO1 deficiency enhances VEGFA N-glycosylation through potentiation of MAGT1, a subunit of the STT3B-containing oligosaccharyltransferase (OST) complex [24], we hypothesized that ERO1 loss may broadly remodel the tumor N-glycoproteome. As our previous studies indicated that ERO1 activity is important for cellular adaptation to hypoxia, a stress condition that perturbs ER redox homeostasis and is physiologically relevant to tumors [19] [44]. We therefore performed the glycoproteomic analysis under hypoxic conditions to determine whether ERO1 deficiency alters the tumor glycoproteome. To identify glycoproteins enriched in ERO1 KO E0771 cells and in their secretome, intracellular proteins (IC) and conditioned media (SEC) from WT and ERO1 KO cells cultured under hypoxic conditions were subjected to lectin-based enrichment using concanavalin A (ConA) or wheat germ agglutinin (WGA) followed by mass spectrometry analysis and label-free quantification (Fig. 2E).

ConA-enriched intracellular and secreted proteins from WT and ERO1 KO cells were analyzed by Coomassie staining (Fig. 2F) and no major differences in total protein abundance or overall protein profiles were observed between the two genotypes (Fig. 2F). However, subsequent mass spectrometry analysis and label-free quantification



(caption on next page)

Fig. 1. ERO1A is highly expressed in TNBC and shows limited association with immune checkpoint expression A) ERO1A protein abundance across PAM50 subtypes, including Basal-like, HER2-enriched, Luminal A, Luminal B tumors and TNBC. Box plots show log2-transformed ERO1A protein abundance; each dot represents an individual sample. The central line indicates the median, the box represents the interquartile range (IQR), and whiskers extend to 1.5 × IQR. Pairwise comparisons with normal breast tissue were performed using the Wilcoxon rank-sum test. B) Scatterplots showing correlations between ERO1A and PD-L1, PD-1 or CTLA-4 protein abundance. Correlations are shown separately for normal breast tissue, all breast cancer samples, and TNBC samples. In the analysis including all breast cancer samples, dots are colored according to PAM50 subtype. Each dot represents an individual sample and is labeled by Study_ID. Linear regression lines are overlaid to illustrate trends, while associations were quantified using Spearman's rank correlation coefficient; the corresponding ρ (rho), P value, and number of evaluated samples are reported in each panel. C) Representative immunofluorescence images of a TMA comprising Luminal A and TNBC breast cancer specimens. PD-1 and PD-L1 expression were assessed by immunofluorescence staining, with nuclei counterstained with Hoechst. Scale bars, 500 and 50 μm. Dot plots on the right show the quantification of PD-1 and PD-L1 fluorescence intensity within the tumor tissue area of the TMA. Each dot represents one tumor sample. D) Scatterplots showing the correlation between ERO1 and PD-L1 or PD-1 expression in Luminal A and TNBC breast tumor samples included in the TMA. Each dot represents one tumor sample. Correlations were assessed using Spearman's rank correlation analysis. Spearman's correlation coefficient (ρ) and P value are shown in each panel.

identified several proteins that were differentially enriched in ERO1 KO cells compared with WT controls. To gain insight into the biological processes affected by ERO1 loss, differentially enriched N-glycosylated proteins were subjected to Reactome pathway enrichment analysis. Among the glycosylated proteins enriched in the secretome of ERO1 KO cells, the Reactome pathways "Extracellular Matrix Organization" and "Innate Immune System" emerged as the most significantly enriched categories compared with WT (Fig. 2G). These findings suggest that ERO1-dependent remodeling of the secreted glycoproteome may affect biological pathways involved in extracellular matrix regulation and tumor–immune communication.

Although PD-L1 was not detected among the intracellular proteins identified in E0771 cells, given its reported regulation by ERO1 and the role of N-glycosylation in modulating PD-L1 function, we next investigated whether ERO1 deficiency affects PD-L1 glycosylation [45] [46]. Analysis of PD-L1 expression revealed that PD-L1 abundance was significantly increased in ERO1 KO cells under hypoxic conditions (Fig. 2H). Treatment with the glycosidases Endo H and PNGase F resulted in mobility shifts of PD-L1, supporting its N-glycosylated state (Fig. 2I). Furthermore, PD-L1 was enriched and detected by Western blot following WGA-mediated lectin pull-down in ERO1 KO cells, supporting increased glycosylation of PD-L1 in hypoxic ERO1 KO E0771 cells (Fig. 2J). Analysis of the ER-localized ratiometric redox sensor roGFP2 showed that ERO1 KO cells were less oxidized than WT cells. Treatment with the reducing agent β-mercaptoethanol (β-ME; 55 μM for 48 h) significantly shifted the ER redox state of both WT and ERO1 KO cells toward more reducing conditions (Fig. 2K). To address the point that increased PD-L1 glycosylation in ERO1 KO cells occurs under less oxidizing ER conditions, we treated WT and ERO1-KO MDA-MB-231 cells, which express higher levels of PD-L1, with β-ME under hypoxic conditions. Glycosylated PD-L1 was enriched by WGA-mediated lectin pull-down and detected by Western blotting, supporting increased PD-L1 glycosylation in hypoxic ERO1 KO cells under more reducing redox conditions (Fig. 2L).

Collectively, these results suggest that ERO1 deficiency increases both PD-L1 abundance and its glycosylation under hypoxic conditions, potentially influencing PD-1/PD-L1 immune checkpoint signaling in TNBC cells.

5.3. Tumor cell–intrinsic ERO1 promotes responsiveness to PD-1 blockade in immune-competent bone marrow chimeric mice

Because ERO1 is expressed in both tumor cells and in immune cell populations within the TME, we next investigated whether its functional contribution to tumor progression originates from tumor cells or from hematopoietic cells of the TME [11]. To address this question, we generated chimeric syngeneic immune-competent mice by transplanting bone marrow cells isolated from WT or ERO1 KO CD45.2 donor mice into lethally irradiated CD45.1 recipient mice [35] (as indicated in the scheme in Fig. 3A).

Efficient hematopoietic reconstitution of the TME was confirmed two weeks after transplantation by flow cytometric analysis of peripheral blood leukocytes, which demonstrated that more than 95% of circulating $CD45^+$ leukocytes were donor-derived CD45.2+ cells (Fig. 3B).

Following hematopoietic reconstitution, WT or ERO1 KO E0771 cells were orthotopically implanted into the mammary fat pad of these chimeric syngeneic immune-competent recipient mice. Tumor growth was then monitored to assess the relative contribution of ERO1 expression in tumor cells versus bone marrow–derived immune cells of the TME (as indicated in the scheme in Fig. 3A).

Under basal conditions, neither ERO1 deficiency in tumor cells nor ERO1 deficiency in hematopoietic bone marrow cells (bm) of the TME significantly affected primary tumor growth compared with WT controls. In addition, hematopoietic compartment with ERO1 KO cells did not alter tumor progression of WT tumors, indicating that ERO1 in the immune cells of the TME did not modulate tumor growth (Fig. 3C).

We next evaluated the impact of ERO1 on responsiveness to immune checkpoint blockade. Tumor-bearing chimeric mice were treated with anti–PD-1 antibody or isotype control once tumors became palpable. WT tumors showed limited responsiveness to PD-1 blockade, regardless of whether the hematopoietic compartment of the TME was WT or ERO1-deficient.

In contrast, ERO1 KO tumors responded robustly to PD-1 blockade, exhibiting markedly reduced tumor growth and, in several cases, complete tumor regression (Fig. 3C and D).

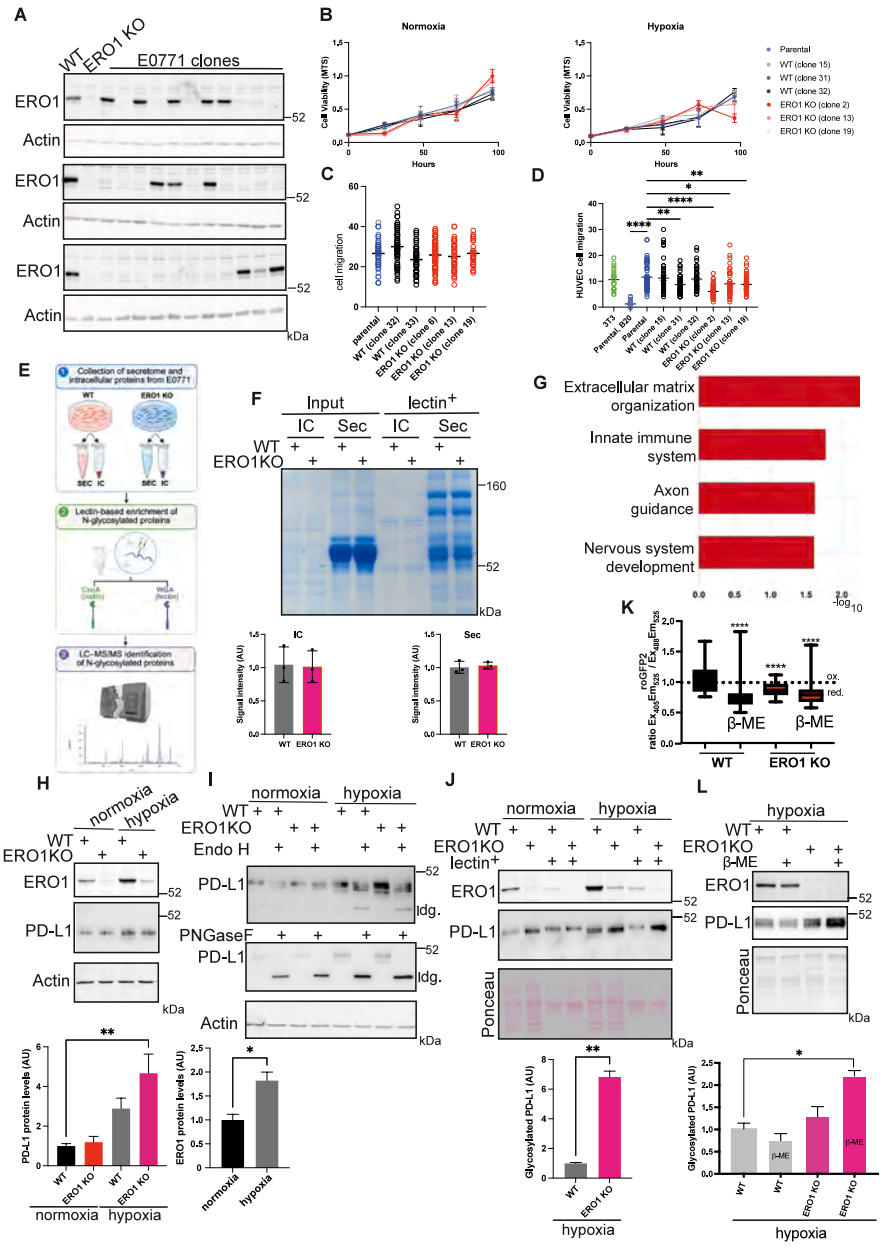
Importantly, this enhanced therapeutic response was observed in chimeric mice reconstituted with either WT or ERO1 KO bone marrow, indicating that the improved sensitivity to PD-1 blockade is primarily driven by ERO1 deficiency in tumor cells rather than by ERO1 deficiency in the hematopoietic compartment of the TME.

5.4. ERO1 deficiency promotes myeloid transcriptional remodeling

To investigate the molecular mechanisms underlying the enhanced responsiveness of ERO1 KO tumors to PD-1 blockade, we performed RNA sequencing on tumors obtained from mice bearing WT or ERO1 KO E0771 tumors and reconstituted with either WT or ERO1 KO bone marrow.

Gene set enrichment analysis (GSEA) revealed significant modulation of pathways associated with PD-1 signaling in ERO1 KO tumors (Fig. 4A). Among the comparisons analyzed, positive enrichment of the PD-1 co-inhibitory pathway was statistically significant in the combined analysis comparing ERO1 KO bm, ERO1 KO tumor samples (derived from mice receiving ERO1 KO bone marrow and bearing ERO1 KO tumors) with WT bm, WT tumor samples (derived from mice receiving WT bone marrow and bearing WT tumors) (Fig. 4A). Gene-level analysis further demonstrated heterogeneous regulation of individual pathway components, with several genes displaying significant differential expression, indicating extensive remodeling of PD-1-associated signaling networks under ERO1-deficient conditions (Fig. 4A).

To determine whether ERO1 deficiency in tumor cells induced broader immune-related transcriptional changes, we compared tumors of the two different genotypes in mice reconstituted with ERO1 KO bone marrow. GSEA identified strong enrichment of immune-related gene sets in ERO1 KO tumors (Fig. 4B). The most significantly enriched signatures



(caption on next page)

included macrophage, monocyte, and dendritic cell programs, as well as pathways involved in antigen processing and presentation.

Consistent with these findings, network analysis restricted to MSigDB M7 immunologic signatures revealed a densely interconnected enrichment landscape characterized by extensive overlap among positively enriched immune gene sets (Fig. 4C). Functional clustering of these signatures identified coordinated modules associated with innate immune responses, antigen presentation, myeloid cell recruitment, inflammatory pathways, and immune checkpoint blockade–related programs. The high degree of connectivity among these modules suggests that ERO1 deficiency in tumors triggers a broad and coordinated activation of immune pathways rather than isolated transcriptional changes.

To determine whether these transcriptional alterations were reflected at the cellular level, we next examined the immune composition of the TME by single-cell analysis. The overall composition of immune cell populations did not differ substantially between tumors from mice reconstituted with WT or ERO1 KO bone marrow (bm) (Fig. 4D). Consistent with the enrichment of myeloid-associated gene signatures identified by RNA sequencing, mice bearing ERO1 KO tumors exhibited increased macrophage frequencies and reduced monocyte representation compared with mice bearing WT tumors, irrespective of bone marrow genotype (Fig. 4E). These cellular findings provide orthogonal validation of the transcriptomic analyses and support the conclusion that ERO1 deficiency remodels the myeloid compartment of the TME. Collectively, the transcriptomic and single-cell analyses demonstrate that tumor cell–intrinsic loss of ERO1 promotes immune remodeling characterized by enhanced antigen presentation, enrichment of macrophage-, monocyte-, and dendritic cell–associated programs, and extensive rewiring of PD-1–associated transcriptional networks. Together, these findings support a model in which ERO1 deficiency establishes a tumor immune microenvironment that is more permissive to anti–PD-1-mediated antitumor immunity.

Fig. 2. ERO1 deficiency remodels the secreted glycoproteome and increases PD-L1 glycosylation in E0771 TNBC cells A) Western blot showing ERO1 expression in WT and CRISPR/Cas9-generated ERO1-KO E0771 clones. B) Cell growth curves of WT and ERO1 KO E0771 cells under normoxic and hypoxic conditions assessed by MTS assay. Data are presented as mean ± SEM. Statistical significance was evaluated using two-way ANOVA (N = 5). C) Dot plots showing the number of WT and ERO1 KO E0771 cells that migrated through Boyden chambers. Migrated cells were quantified in ten randomly selected fields from three independent migration assays for each clone. Statistical significance was evaluated using one-way ANOVA. D) Dot plots showing the number of HUVECs that migrated toward conditioned media derived from WT and ERO1 KO E0771 cells. Conditioned medium from NIH3T3 fibroblasts was used as a positive chemoattractant control. Where indicated, conditioned media were pre-incubated with the VEGF antibody B20 to neutralize VEGF before being used in migration assays. Parental refers to the original E0771 cell line. Statistical significance was determined using one-way ANOVA. E) Schematic representation of the experimental workflow used for N-glycoproteome analysis. Intracellular proteins (IC) and conditioned media (Sec) from WT and ERO1 KO E0771 cells cultured under hypoxic conditions were subjected to lectin-based enrichment using concanavalin A (ConA) or wheat germ agglutinin (WGA), followed by LC-MS/MS analysis and label-free quantification. F) Coomassie staining of input and N-glycosylated proteins (lectin$^+$) isolated from WT and ERO1 KO E0771 cells. Intracellular and conditioned medium fractions enriched using ConA were analyzed by SDS–PAGE. Below, the accompanying bar graphs show total protein abundance following ConA enrichment. Data are presented as mean ± SEM. Statistical significance was assessed using an unpaired two-tailed Student's *t*-test (N = 3). G) Reactome pathway enrichment analysis of differentially enriched N-glycosylated proteins from ERO1 KO cells relative to WT controls identified by LC–MS/MS from conditioned media. Pathways with an adjusted P value < 0.05 were considered significantly enriched and are displayed. H) Representative Western blots showing ERO1 and PD-L1 expression in WT and ERO1 KO E0771 cells cultured under normoxic or hypoxic conditions. Quantification of PD-L1 and ERO1 protein levels is shown below the blots. Data are presented as mean ± SEM. Statistical significance was assessed using one-Way ANOVA and unpaired two-tailed Student's *t*-test respectively (N = 3). I) Western blot analysis of PD-L1 following digestion with PNGase F or Endo H in WT and ERO1 KO E0771 cells, demonstrating changes in electrophoretic mobility associated with N-glycosylation. Dg., deglycosylated protein band. J) WGA lectin (lectin$^+$) pull-down assay and the correspondent input in WT and ERO1 KO E0771 cells. Quantification of glycosylated PD-L1 protein levels is shown below the blots. Data are presented as mean ± SEM. Statistical significance was assessed using an unpaired two-tailed Student's *t*-test (N = 3). K) Bar plots showing the baseline fluorescence excitation ratio of the ER-localized ratiometric redox sensor roGFP2 in WT and ERO1 KO HeLa cells following treatment with β-mercaptoethanol (β-ME). Data are presented as mean ± SEM (N = 4 fields of view). Statistical significance relative to WT was assessed by one-way ANOVA. L) WGA-mediated lectin pull-down assay in WT and ERO1 KO MDA-MB-231 cells. Quantification of glycosylated PD-L1 levels is shown below the blots. Data are presented as mean ± SEM (N = 3). Statistical significance was assessed by one-way ANOVA.

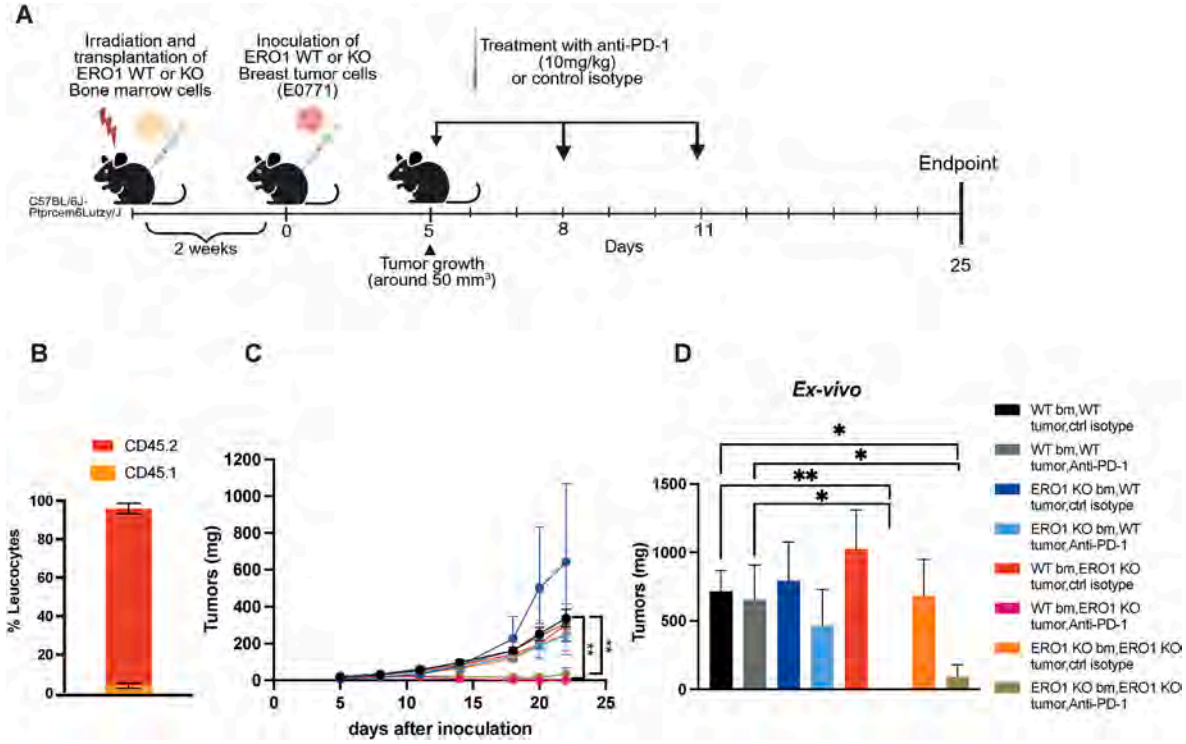
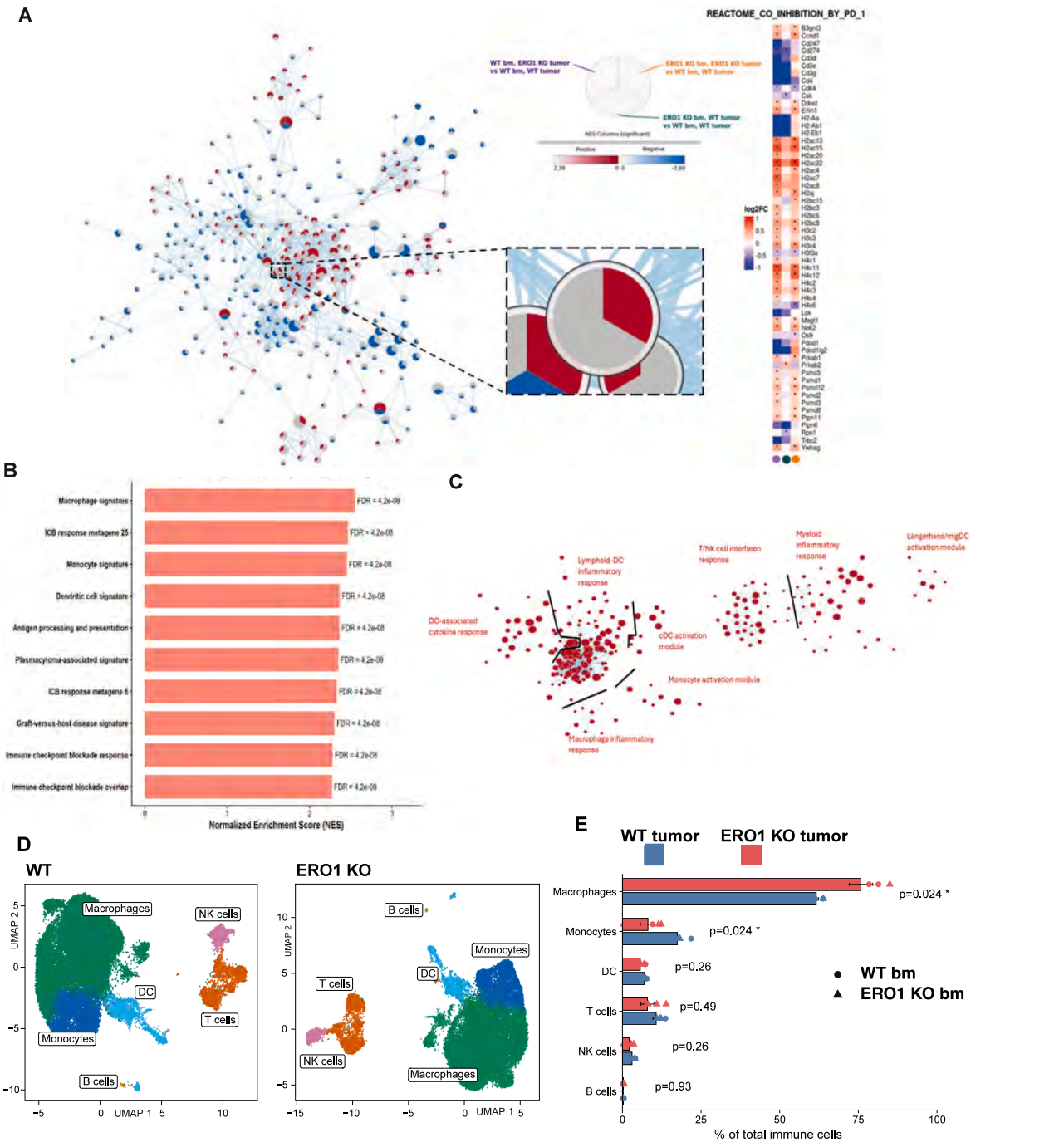


Fig. 3. Tumor–intrinsic ERO1 deficiency promotes responsiveness to PD-1 blockade in bone marrow chimeric mice. A) Experimental scheme illustrating the generation of bone marrow chimeric mice. Bone marrow cells isolated from WT or ERO1 KO CD45.2 donor mice were transplanted into lethally irradiated CD45.1 recipient mice. Following hematopoietic reconstitution, WT or ERO1 KO E0771 cells were orthotopically implanted into the mammary fat pad, and mice were subsequently treated with anti–PD-1 antibody or control isotype as indicated. B) Representative flow cytometry analysis of peripheral blood showing hematopoietic reconstitution in recipient mice two weeks after bone marrow transplantation. Donor-derived CD45.2$^+$ cells represented 95% of circulating CD45$^+$ leukocytes. C) Tumor growth curves of WT and ERO1 KO E0771 tumors implanted into chimeric mice reconstituted with either WT or ERO1 KO bone marrow and treated with anti–PD-1 antibody or isotype control. Tumor volumes were monitored over 25 days after tumor cell implantation. Data are presented as mean ± SEM. Statistical significance was determined by two-way ANOVA with Sidak's multiple-comparisons test (N = 12 mice for conditions). D) Ex-vivo individual tumor weight at endpoint. Statistical significance was determined by one-way ANOVA.

5.5. ERO1-deficient tumors exhibit increased myeloid infiltration and PD-1 expression

To further refine the changes observed within the myeloid compartment by transcriptomic and single-cell analyses, we performed multiparametric flow cytometric profiling of orthotopic WT and ERO1 KO E0771 tumors from chimeric mice reconstituted with either WT or ERO1 KO bone marrow.

Analysis of the lymphoid compartment revealed no major differences among the different conditions (Fig. 5A), whereas myeloid compartment



(caption on next page)

demonstrated a significant increase in tumor-infiltrating dendritic and neutrophilic cells within ERO1 KO tumors compared with WT counterparts (Fig. 5B). The expansion of dendritic cells was observed irrespective of the genotype of the transplanted bone marrow whereas neutrophils increased only in ERO1 KO tumors from mice reconstituted with WT bone marrow. Immunofluorescence analysis of PD-1 and PD-L1 expression in WT and ERO1 KO tumor sections revealed a significant increase in PD-1 staining in ERO1 KO tumors, whereas PD-L1 expression remained unchanged (Fig. 5C).

Together, these findings further support a role for ERO1 deficiency in shaping the immune microenvironment by promoting myeloid cell remodeling and increasing PD-1 expression, providing additional evidence that loss of ERO1 establishes a tumor milieu more responsive to PD-1 blockade.

5.6. *Pharmacological ERO1 inhibition phenocopies ERO1-deficient tumors*

To determine whether pharmacological inhibition of ERO1 could reproduce the immune-responsive phenotype observed in ERO1-deficient tumors, WT bone marrow chimeric mice bearing orthotopically implanted WT E0771 tumors were treated with our novel ERO1 inhibitor I29 followed by anti-PD-1 therapy [38]. As a reference, WT bone marrow chimeric mice bearing ERO1 KO E0771 tumors were treated with anti-PD-1 according to the same experimental schedule. I29 treatment was initiated three days after tumor implantation, whereas

Fig. 4. ERO1 deficiency promotes immune transcriptional remodeling of the myeloid compartment and PD-1 pathway A) Cytoscape Enrichment Map network and gene level representation of the Reactome co-inhibition by PD-1 pathways across knockouts versus wild-type comparisons. The network highlights the REACTOME_CO_INHIBITION_BY_PD_1 pathway and its connectivity within the interaction map. Each node represents a pathway, while edges indicate gene overlap between pathways, as shared gene sets. In the middle section, nodes are displayed as pie charts, where each sector corresponds to one comparison and the color of each sector reflects the normalized enrichment score (NES), with red indicating positive enrichment and blue indicating negative enrichment. The heatmap on the right reports gene-level log2 fold-change values for the pathway across the same comparisons. Genes marked with an asterisk (*) are significantly differentially expressed (N = 4 for conditions). B) The bar plot shows the top 10 upregulated gene sets identified by GSEA in the ERO1 KO bm, ERO1 KO tumor using MSigDB mouse MH, M2, M5, M7, and M8 gene-set collections. Bar length indicates the normalized enrichment score (NES), while FDR values indicate multiple-testing-adjusted significance. The corresponding pathway annotations are listed below. ZHANG UTERUS C5 MACROPHAGE = Macrophage signature, ZENG GU ICB CONTROL METAGENE 25 PRECICTIVE ICB RESPONSE = ICB response metagene 25, HANG UTERUS C12 MONOCYTE = Monocyte signature, ZHANG UTERUS C9 DENDRITIC CELL = Dendritic cell signature, GOBP ANTIGEN PROCESSING AND PRESENTATION = Antigen processing and presentation, QI PLASMACYTOMA UP = Plasmacytoma-associated signature, ZENG GU ICB CONTROL METAGENE 8 PRECICTIVE ICB RESPONSE = ICB response metagene 8, ICHIBA GRAFT VERSUS HOST DISEASE D7 UP = Graft-versus-host disease signature, ZEMEK IMMUNE CHECKPOINT BLOCKADE OVARIAN CANCER RENCA UP = Immune checkpoint blockade response, ZEMEK IMMUNE CHECKPOINT BLOCKADE OVARIAN CANCER OVERLAP UP = Immune checkpoint blockade overlap. C) Cytoscape Enrichment Map visualization of GSEA results restricted to MSigDB mouse M7 Immunologic signature gene sets in the above comparison. Nodes represent positively enriched immunologic gene sets and edges indicate gene-set similarity based on shared leading-edge genes. Node size reflects gene-set size, while edge thickness and intensity represent the degree of overlap between gene sets. The network highlights coordinated activation of immune and inflammatory programs. Red labels summarize manually curated biological themes assigned to each enrichment module. D) Single-cell RNA sequencing analysis of tumor-infiltrating immune cells from WT and ERO1 KO tumors developing in mice reconstituted with either WT or ERO1 KO bone marrow (bm). UMAP projection showing the distribution of major immune cell populations identified across mice with wild-type bone marrow or ERO1-deficient bone marrow. Cell clusters were colored based on broad immune annotations, including macrophages, monocytes, dendritic cells (DC), T cells, natural killer (NK) cells, natural killer T (NKT) cells and B cells. E) Quantification of immune cell populations identified by single-cell RNA sequencing. Bar plots show the relative abundance of immune cells within WT and ERO1 KO tumors, including samples from both WT and ERO1 KO bone marrow-bearing mice. Point shapes indicate the bone marrow genotype of each sample. Data are presented as mean ± SEM. P-values were calculated using a two-sided Wilcoxon rank-sum test (WT tumors, N = 6 mice; ERO1 KO tumors, N = 5 mice) and adjusted using the Benjamini–Hochberg method. Adjusted p-values are shown in the figure.

anti-PD-1 administration was started two days later, as indicated in Fig. 6A. I29 was administered every two days until day 25 for a total of eleven times, while anti-PD-1 was delivered three times.

Tumor growth analysis revealed that WT tumors treated with the combination of I29 and anti-PD-1 displayed reduced growth compared with WT tumors treated with I29 alone. Importantly, the growth kinetics of WT tumors receiving the combined I29 and anti-PD-1 treatment closely mirrored those observed in ERO1 KO tumors treated with anti-PD-1 (Fig. 6B).

Magnetic resonance imaging (MRI) analysis of tumor-bearing mice confirmed the therapeutic benefit of combining ERO1 inhibition with PD-1 blockade, as evidenced by the significant reduction in tumor volume (Fig. 6C), indicating that pharmacological inhibition of ERO1 with I29 restores responsiveness to anti-PD-1 therapy and mirrors the effect on ERO1 KO tumors.

To determine whether pharmacological ERO1 inhibition also reproduced the myeloid immune remodeling associated with tumor-intrinsic ERO1 deficiency, tumors were subjected to multiparametric flow cytometric analysis. Like ERO1 KO tumors, I29-treated WT tumors did not exhibit major differences in lymphoid cell populations (Fig. 6D) but showed increased infiltration of dendritic cells together with increased neutrophil accumulation within the TME (Fig. 6E). These findings recapitulate the overall myeloid alterations observed following genetic ERO1 ablation in the tumor.

Collectively, these results suggest that pharmacological inhibition of ERO1 reproduces both the enhanced responsiveness to PD-1 blockade and the myeloid immune remodeling associated with tumor cell-intrinsic ERO1 deficiency, thereby identifying ERO1 as a therapeutically actionable target for improving the efficacy of immune checkpoint blockade in TNBC.

5.7. ERO1 deficiency confers durable sensitivity to PD-1 blockade in immunocompetent mice

To validate the results obtained in bone marrow chimeric mice, we next assessed the therapeutic response to PD-1 blockade in a conventional orthotopic breast cancer mouse model. Thus, WT and ERO1 KO E0771 cells were implanted into the mammary fat pad of immunocompetent C57BL/6 J mice, and anti–PD-1 treatment was initiated once tumors became palpable, five days after implantation (Fig. 7A).

Consistent with the results obtained in chimeric mice, WT tumors displayed only limited sensitivity to PD-1 blockade and continued to progress throughout the observation period (25 days). In contrast, ERO1 KO tumors exhibited an even more striking response than that observed in chimeric mice to anti–PD-1 therapy, characterized by both inhibition of tumor growth and progressive tumor regression. By day 25 after tumor cell transplantation, tumor growth was almost completely suppressed in most mice bearing ERO1 KO tumors, as further confirmed by ex vivo tumor measurements at the endpoint (Fig. 7B and C). To determine the durability of this response, mice that had achieved complete tumor regression were monitored for an additional 20 days. Notably, no tumor recurrence was observed during the follow-up period, indicating long-lasting therapeutic efficacy following PD-1 blockade in mice bearing ERO1 KO tumors (Fig. 7B).

To investigate the immune cells associated with this enhanced response, tumors were analyzed by flow cytometry at the experimental endpoint. Analysis of the lymphoid compartment revealed a marked increase in activated cytotoxic T-cell populations in ERO1 KO tumors including increased PD-1-expressing $CD8^+$ T cells, together with elevated proportions of granzyme B (GrzB)–positive $CD8^+$ T cells and NK cells, compared with WT tumors (Fig. 7D). These findings are consistent with enhanced activation and effector differentiation of cytotoxic lymphocytes within the ERO1-deficient TME.

Analysis of the myeloid compartment demonstrated a concomitant increase in tumor-infiltrating neutrophils in ERO1 KO tumors, like that observed in the chimeric mouse model (Fig. 7E). Moreover, neutrophils in ERO1 KO tumors exhibited higher levels of PD-L1 expression compared with those from WT tumors (Fig. 7E). The increase in neutrophils was also observed in the two ERO1 KO tumors that remained detectable after anti–PD-1 treatment, suggesting that activation of the neutrophil compartment represents a consistent feature of ERO1-deficient tumors.

These data further demonstrate that tumor cell-intrinsic ERO1 shapes the immune landscape of the TME and acts as a critical determinant of responsiveness to immune checkpoint inhibition.

6. Discussion

The present study identifies ERO1, an UPR-associated ER oxidoreductase, as a key regulator of tumor immunogenicity and responsiveness to immune checkpoint blockade in TNBC. Although ERO1 has been mainly studied for its role in oxidative protein folding [35], adaptation

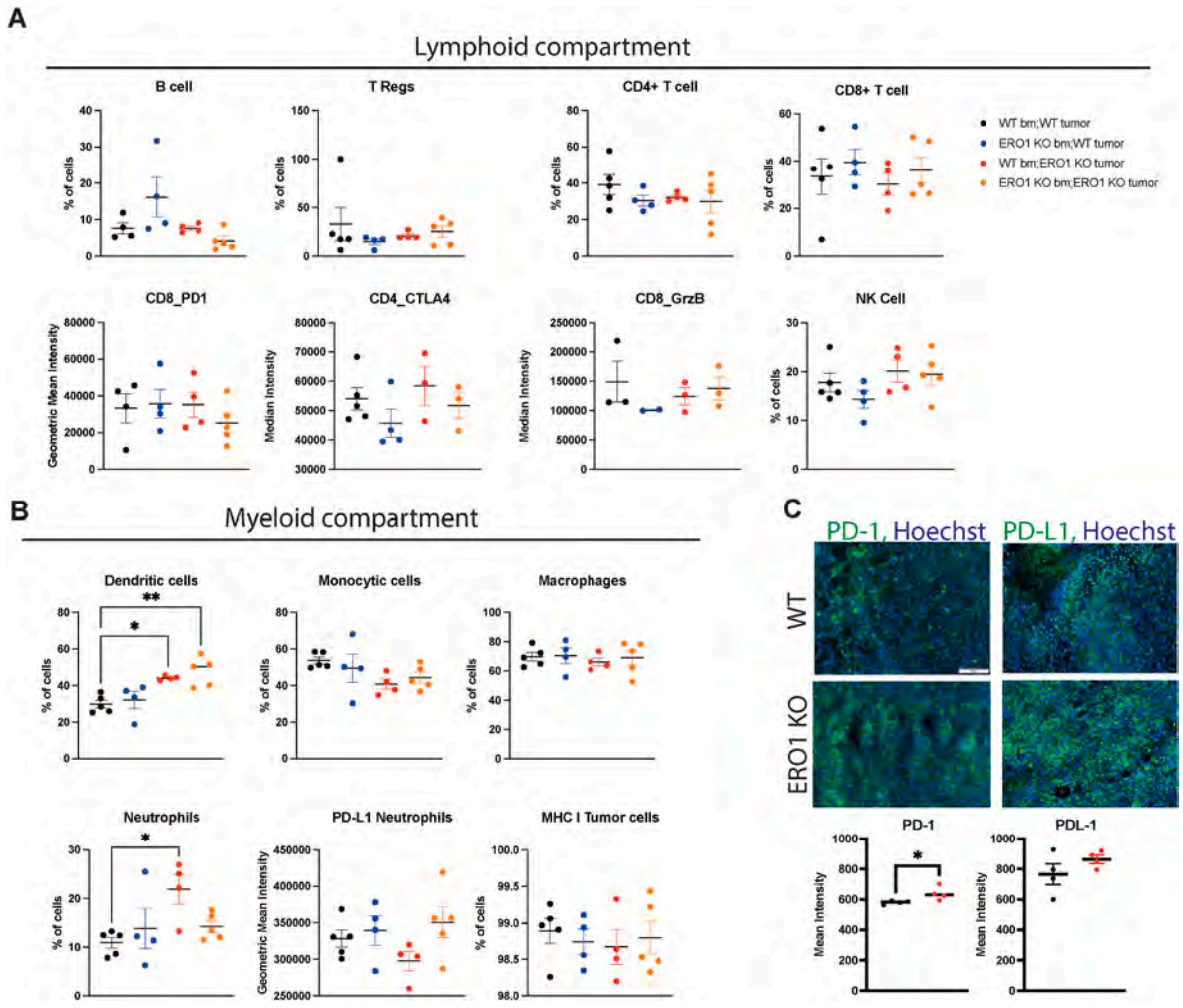


Fig. 5. ERO1 deficiency remodels the myeloid compartment and increases PD-1 expression A) Dot plots showing the frequencies of the indicated lymphoid cell populations in orthotopic WT and ERO1 KO E0771 tumors growing in chimeric mice reconstituted with either WT or ERO1 KO bone marrow (bm). B) Dot plots showing the frequencies of the indicated myeloid cell populations in WT and ERO1 KO E0771 tumors from chimeric mice reconstituted with WT or ERO1 KO bone marrow. Data presented in A and B are presented as mean ± SEM. Statistical significance was determined using one-way ANOVA. C) Representative immunofluorescence images of WT and ERO1 KO tumor sections stained for PD-1 and PD-L1. Nuclei were counterstained with Hoechst. Dot plots below show the quantification of PD-1 and PD-L1 fluorescence signals within the tumor area. Data are presented as mean ± SEM. Statistical significance was determined using an unpaired two-tailed Student's *t*-test.

to ER stress, and tumor progression [15], our findings demonstrate that ERO1 also modulates antitumor immunity through tumor cell–intrinsic mechanisms linked to ER redox and protein glycosylation, thereby promoting a more immune-active TME in TNBC that is consistent with enhanced antigen-presentation programs and immune surveillance [47].

The UPR, through its three principal branches—IRE1, PERK, and ATF6—supports tumor adaptation and survival by regulating both cancer cell–intrinsic and TME-dependent mechanisms that shape antitumor immunity [48] [49,50] [5,51–54]. Accordingly, both tumor cells and the TME engage UPR signaling to regulate immune infiltration, immune evasion, and responses to immunotherapy [55] [56].

ERO1 genetic deletion has been shown to enhance the response to anti–PD-1 therapy in colon carcinoma, lung adenocarcinoma, and melanoma models by improving T-cell function [14]. Here, we provide mechanistic evidence linking tumor-intrinsic ERO1 activity to immune checkpoint responsiveness in TNBC.

TNBC is characterized by constitutive ER stress and persistent activation of the UPR, which facilitates tumor resilience under hostile microenvironmental conditions and promotes therapy resistance [1,3,5,57]. TNBC is also one of the few breast cancer subtypes for which immune checkpoint blockade has shown clinical benefit. However, its limited efficacy in TNBC underscores the need to identify mechanisms that augment immune responses [2].

Building on our previous observations that ERO1 deficiency alters the N-glycosylation of VEGF through enhanced activity of the OST subunit MAGT1 [13,24,29,38] [19] [58], we hypothesized that ERO1 deficiency might exert broader effects on the tumor glycoproteome. Our previous studies indicated that ERO1 deficiency shifts the ER toward a more reduced redox poise, thereby enhancing MAGT1-dependent glycosylation of cysteine-proximal acceptor sites [24], consistent with evidence that the thioredoxin domain of MAGT1 regulates N-glycosylation and that reductive pathways can contribute to efficient N-glycosylation [25] [26]. In the present study, glycoproteomic analysis of lectin-enriched secreted proteins from ERO1-deficient E0771 breast cancer cells revealed proteins involved in immune-related pathways. MAGT1 was also upregulated in the RNA sequencing analysis of ERO1-deficient E0771 breast tumors and was associated with the Reactome "Coinhibition by PD-1" pathway. Together, these observations support a model in which ERO1 loss–induced redox remodeling may influence the tumor immune glycoproteome through MAGT1. Given the established role of glycosylation in regulating antigen

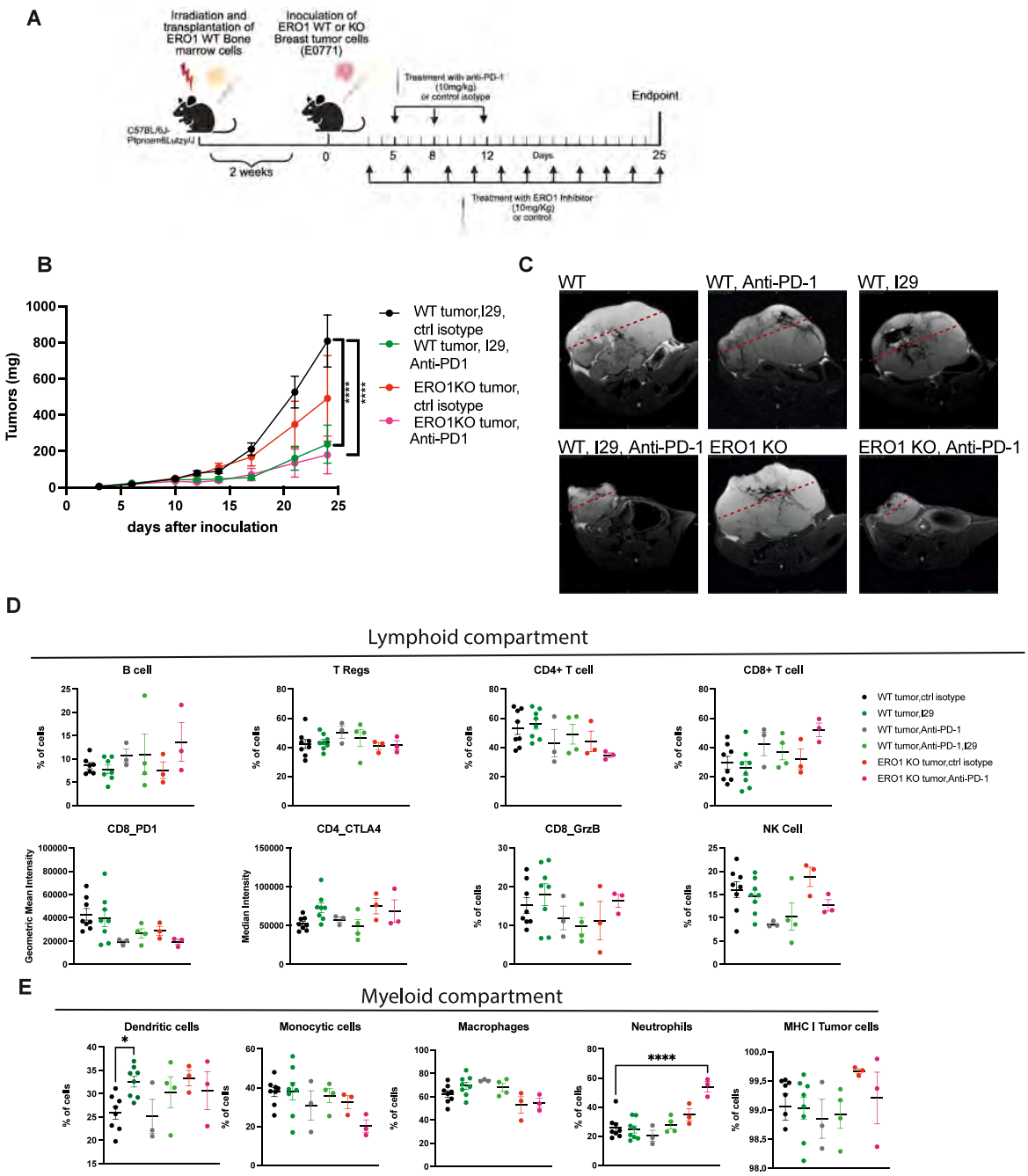


Fig. 6. Pharmacological ERO1 inhibition phenocopies ERO1-deficient tumors. A) Experimental design. WT bone marrow chimeric mice bearing orthotopically implanted WT E0771 tumors were treated with the ERO1 inhibitor I29 alone or in combination with anti–PD-1 antibody. As a reference group, mice bearing ERO1 KO E0771 tumors received anti–PD-1 treatment according to the same schedule. I29 administration was initiated 3 days after tumor implantation and repeated every 2 days until day 25. Anti–PD-1 treatment was started 5 days after tumor implantation and administered three times as indicated. B) Tumor growth curves of WT E0771 tumors treated with isotype control, I29, or I29 plus anti–PD-1, and ERO1 KO E0771 tumors treated with anti–PD-1 or isotype control (N = 10 mice for conditions). Statistical significance was determined using two-way ANOVA with Sidak's multiple-comparisons test. C) Representative magnetic resonance imaging (MRI) scans and quantification of tumor volume at the experimental endpoint. The dashed red line indicates the diameter of the tumor. D) Dot plots showing the frequencies of the indicated lymphoid cell populations. E) Dot plots showing the frequencies of the indicated myeloid cell populations in tumors from the different treatment groups. Data in panels D and E are presented as mean ± SEM. Statistical significance was determined using one-way ANOVA.

presentation and immune recognition, including through the PD-1/PD-L1 immune checkpoint axis, these findings suggest that ERO1-dependent glycoproteome remodeling might influence tumor immunogenicity and responsiveness to immune checkpoint blockade [43,59]. To determine whether these effects were driven by ERO1 deficiency in tumor cells or also in the immune compartment of the TME, we performed bone marrow transplantation studies in immunocompetent tumor-bearing mice. While neither tumor-specific nor hematopoietic ERO1 deletion substantially affected primary tumor growth under basal conditions, loss of ERO1 in tumor cells markedly and persistently enhanced the therapeutic efficacy of PD-1 blockade. Thus, these findings support a predominantly tumor-intrinsic role for ERO1 in regulating immunotherapy responsiveness.

The increased myeloid-cell infiltration of ERO1-KO tumors, together with the enrichment of antigen-processing and antigen-presentation pathways observed by RNA sequencing, is consistent with a more

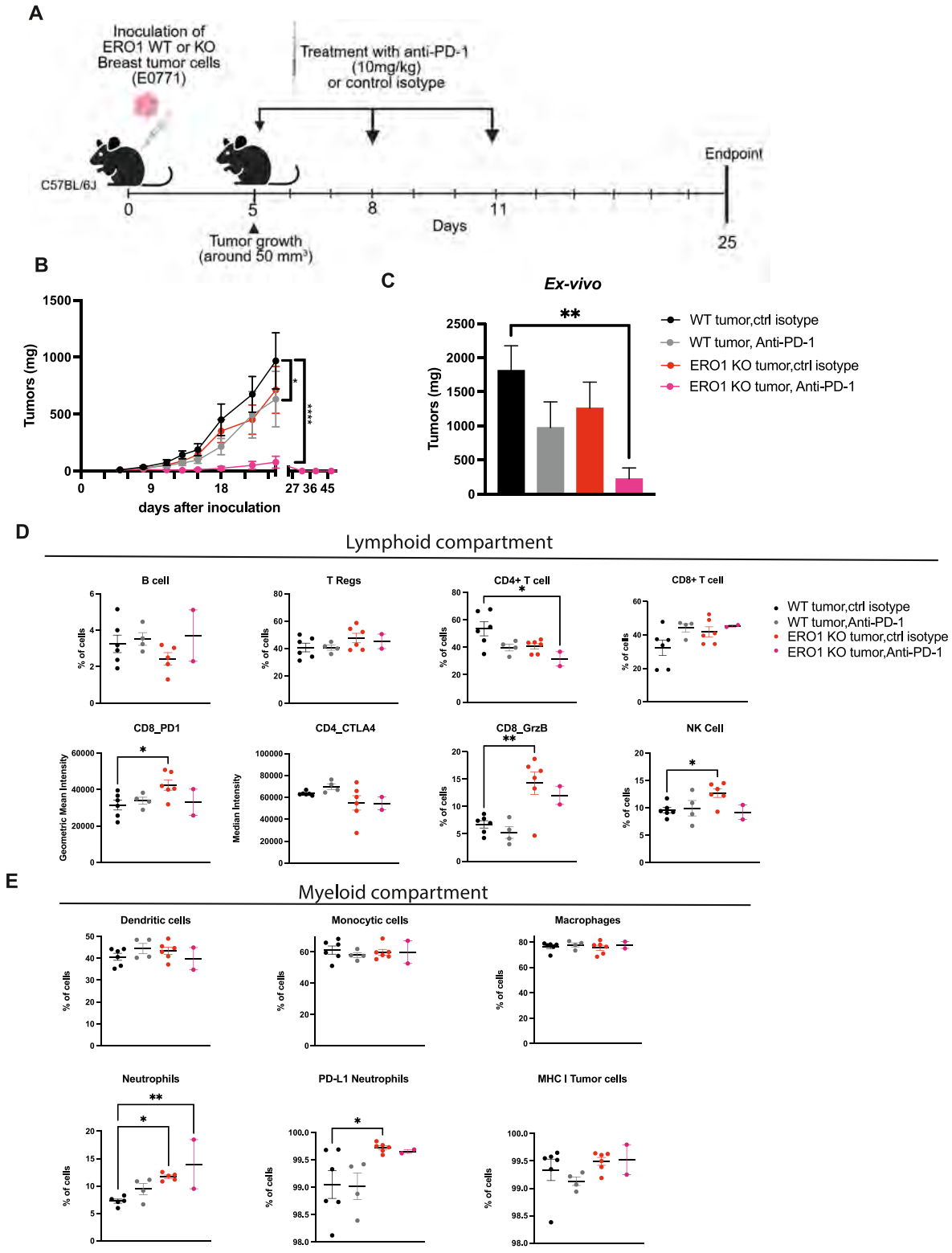


Fig. 7. Tumor-intrinsic ERO1 deficiency confers durable effect to PD-1 blockade in immunocompetent mice. A) Experimental scheme. WT and ERO1 KO E0771 cells were orthotopically implanted into the mammary fat pad of immunocompetent C57BL/6 J mice. Anti–PD-1 treatment was initiated 5 days after tumor implantation, when tumors became palpable, according to the schedule indicated. B) Tumor growth curves of WT and ERO1 KO E0771 tumors treated with anti–PD-1 antibody and followed for 25 days. Mice achieving complete tumor regression were monitored for an additional 20 days to assess tumor recurrence. Statistical significance was determined using two-way ANOVA with Sidak's multiple-comparisons test. C) Endpoint tumor burden determined by ex vivo tumor measurements at sacrifice. Data are presented as mean ± SEM. Statistical significance was determined using one-way ANOVA. D) Dot plots showing the frequencies of the indicated lymphoid cell populations. E) Dot plots showing the frequencies of myeloid cell populations within WT and ERO1 KO tumors at the experimental endpoint. Data in panels D and E are presented as mean ± SEM. Statistical significance was determined using one-way ANOVA.

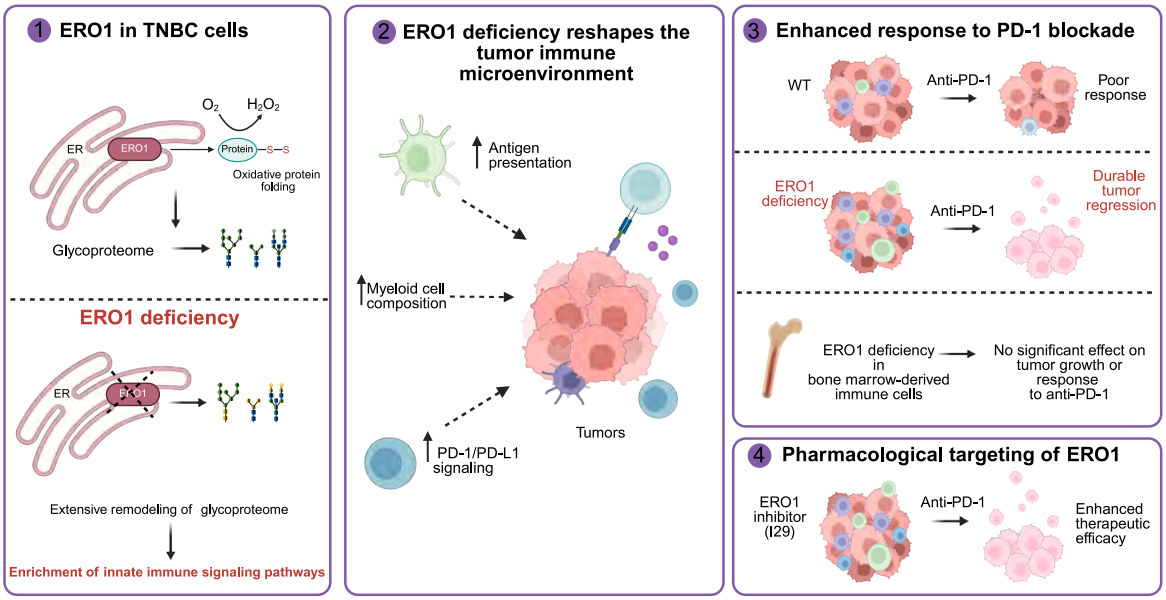


Fig. 8. ERO1 acts as a tumor–intrinsic regulator of tumor immunosurveillance in TNBC. ERO1 is a key mediator of oxidative protein folding and a component of the UPR, an adaptive pathway that promotes TNBC survival under conditions of cellular stress. Loss of ERO1 impinges on ER oxidative poise and remodels the tumor N-glycoproteome thereby promoting immune signaling [1]. This consists of enhanced antigen-presentation programs, remodeling of the myeloid compartment, and modulation of PD-1/PD-L1–associated pathways within the TME [2]. These changes convert otherwise immune-refractory TNBC tumors into a more immune-responsive state and sensitize them to PD-1 blockade. In contrast, ERO1 deficiency in bone marrow–derived cells does not significantly affect tumor growth or responsiveness to PD-1 blockade, demonstrating that the immunomodulatory effects of ERO1 are predominantly tumor cell intrinsic [3]. Pharmacological inhibition of ERO1 with the small-molecule inhibitor I29 phenocopies the effects of genetic ERO1 deletion and enhances the efficacy of immune checkpoint blockade [4].

immunologically active myeloid compartment. Together with the enrichment of immune checkpoint blockade response signatures, these data support a model of a more immunologically active microenvironment in ERO1-deficient tumors and may underlie the enhanced responsiveness of ERO1-deficient tumors to PD-1 blockade [60]. These changes are consistent with the conversion of a relatively immune-refractory tumor state into a more immune-active and checkpoint-responsive TNBC microenvironment. Thus, our findings support the notion that ERO1-dependent tumor glycoproteome remodeling modulates proteins involved in antigen presentation and immune signaling, thereby promoting tumor immune surveillance.

Importantly, pharmacological inhibition of ERO1 using the novel inhibitor I29 recapitulated the effects of genetic ERO1 deletion [29,38] [61]. Indeed, treatment with I29 enhanced the efficacy of anti–PD-1 therapy and reduced tumor burden in immunocompetent hosts, providing proof-of-concept evidence that ERO1 is a therapeutically actionable target in TNBC (Fig. 8/model).

7. Conclusion

Overall, our study identifies ERO1 as a critical regulator of tumor immunogenicity and immune checkpoint responsiveness in TNBC. By linking ER redox and glycoproteome remodeling to the regulation of tumor–immune interactions, our findings expand the understanding of how UPR, through ERO1, contributes to immune evasion. We demonstrate that genetic deletion or pharmacological inhibition of ERO1 enhances antitumor immunity and sensitizes TNBC tumors to anti–PD-1 therapy. These effects are associated with altered ER redox, tumor glycosylation, enhanced antigen presentation, and remodeling of the tumor myeloid compartment toward a more immune-active state. Together, these findings establish a mechanistic connection between ERO1-mediated glycoproteome remodeling in tumor and immune surveillance within the TME and support ERO1 as a promising therapeutic target to enhance the efficacy of immune checkpoint blockade in TNBC.

CRediT authorship contribution statement

Alessandro Cherubini: Investigation. **Ersilia Varone:** Investigation. **Sara Irene Malandrin:** Data curation. **Alice Marrazza:** Formal analysis. **Giorgia Maria Renna:** Conceptualization. **Serena Germani:** Data curation. **Stefano Fumagalli:** Formal analysis. **Angela Bachi:** Methodology. **Angela Cattaneo:** Formal analysis. **Michele Retini:** Methodology. **Giovanni Piersanti:** Methodology. **Marco Bolis:** Formal analysis. **Ilaria Craparotta:** Investigation. **Arianna Vallerga:** Data curation. **Chiara Grasselli:** Methodology. **Manuela Milani:** Resources. **Daniele Generali:** Resources. **Augusto Bleve:** Data curation. **Ester Zito:** Conceptualization, Funding acquisition, Visualization, Writing – original draft.

Ethics approval and consent to participate

Human studies were conducted in accordance with approval from the local ethical committee of "Azienda Socio-Sanitaria Territoriale of Cremona" (RaLCTrVs1Ott_2000). Mouse studies are reported in compliance with the ARRIVE guidelines and conducted in conformity with the following laws, regulations and policies governing the care and use of laboratory animals: Italian Governing Law (D.lgs 26/2014, authorization 19/2008-A issued 6 March 2008 by Ministry of Health; authorization 896/2023-PR and 28/2025-PR issued to E. Zito); Mario Negri Institutional Regulations and Policies providing internal authorization for people conducting animal experiments (Quality Management System Certificate—UNI EN ISO9001: 2008—registration number 6121); EU directives and guidelines (EEC Council Directive 2010/63/UE).

Data availability

The RNA-sequencing data generated in this study have been submitted to the NCBI Gene Expression Omnibus (GEO) [62] [63] under the Superseries accession number GSE337796. This Superseries includes the

bulk RNA-seq dataset (Subseries GSE337795) and the single-cell RNA-seq dataset (Subseries GSE336881). The data are currently available to reviewers by using the code ahwpiwemvdwznkb and will be made publicly accessible upon publication. The mass spectrometry proteomics data have been deposited to the ProteomeXchange Consortium via the PRIDE partner repository with the dataset identifier PXD079823 [64].

Funding

This study was supported by AIRC IG 28733 and Giving Strength to EZ.

Declaration of competing interest

The authors declare that they have no known competing financial interests or personal relationships that could have appeared to influence the work reported in this paper.

Acknowledgments

We are grateful to Prof. Gyorgy Hajnoczky for his critical discussion of the manuscript. We thank Edoardo Micotti for his assistance with MRI. We acknowledge the CINECA award under the ELIXIR-V initiative, for the availability of high-performance computing resources and support.

Abbreviations

ATF6	Activating Transcription Factor 6
ER	Endoplasmic Reticulum
ERO1	Endoplasmic oxidoreductin 1
IRE1	Inositol-requiring enzyme
PDI	Protein Disulfide Isomerase
PD-1	Protein Death 1
PD-L1	Protein death Ligand 1
PERK	Protein Kinase RNA-like Endoplasmic Reticulum Kinase
TME	Tumor microenvironment
TNBC	Triple-negative breast cancer
UPR	Unfolded protein Response
VEGF	Vascular Endothelial growth factor

Appendix A. Supplementary data

Supplementary data to this article can be found online at https://doi.org/10.1016/j.redox.2026.104451.

References

[1] A.C. Garrido-Castro, N.U. Lin, K. Polyak, Insights into molecular classifications of triple-negative breast cancer: improving patient selection for treatment, Cancer Discov. 9 (2) (2019) 176–198.
[2] P. Schmid, S. Adams, H.S. Rugo, A. Schneeweiss, C.H. Barrios, H. Iwata, et al., Atezolizumab and Nab-paclitaxel in advanced triple-negative breast cancer, N. Engl. J. Med. 379 (22) (2018) 2108–2121.
[3] S. Adams, S. Loi, D. Toppmeyer, D.W. Cescon, M. De Laurentiis, R. Nanda, et al., Pembrolizumab monotherapy for previously untreated, PD-L1-positive, metastatic triple-negative breast cancer: cohort B of the phase II KEYNOTE-086 study, Ann. Oncol. 30 (3) (2019) 405–411.
[4] S.L. Topalian, J.M. Taube, R.A. Anders, D.M. Pardoll, Mechanism-driven biomarkers to guide immune checkpoint blockade in cancer therapy, Nat. Rev. Cancer 16 (5) (2016) 275–287.
[5] J.M. Harnoss, A. Le Thomas, M. Reichelt, O. Guttman, T.D. Wu, S.A. Marsters, et al., IRE1alpha disruption in triple-negative breast cancer cooperates with antiangiogenic therapy by reversing ER stress adaptation and remodeling the tumor microenvironment, Cancer Res. 80 (11) (2020) 2368–2379.
[6] E. Zito, G. Hajnoczky, Crosstalk between UPR and mitochondria: the Triad of ER-Mitochondria contacts, Ca(2)(+), and ROS, Pharmacol. Res. (2026) 108428.
[7] B.G. Wouters, M. Koritzinsky, Hypoxia signalling through mTOR and the unfolded protein response in cancer, Nat. Rev. Cancer 8 (11) (2008) 851–864.
[8] A. Cherubini, E. Zito, ER stress as a trigger of UPR and ER-phagy in cancer growth and spread, Front. Oncol. 12 (2022) 997235.
[9] C. Salvagno, J.K. Mandula, P.C. Rodriguez, J.R. Cubillos-Ruiz, Decoding endoplasmic reticulum stress signals in cancer cells and antitumor immunity, Trends Cancer 8 (11) (2022) 930–943.
[10] A. Bassot, J. Chen, K. Takahashi-Yamashiro, M.C. Yap, C.S. Gibhardt, G.N.T. Le, et al., The endoplasmic reticulum kinase PERK interacts with the oxidoreductase ERO1 to metabolically adapt mitochondria, Cell Rep. 42 (1) (2023) 111899.
[11] M.G. Pollard, K.J. Travers, J.S. Weissman, Ero1p: a novel and ubiquitous protein with an essential role in oxidative protein folding in the endoplasmic reticulum, Mol. Cell 1 (2) (1998) 171–182.
[12] A.R. Frand, C.A. Kaiser, The ERO1 gene of yeast is required for oxidation of protein dithiols in the endoplasmic reticulum, Mol. Cell 1 (2) (1998) 161–170.
[13] E. Zito, L. Guarrera, Y.M.W. Janssen-Heininger, Fingerprint of the oxido-reductase ERO1: a protein disulfide bond producer and supporter of cancer, Biochim. Biophys. Acta Rev. Canc 1879 (1) (2023) 189027.
[14] L. Liu, S. Li, Y. Qu, H. Bai, X. Pan, J. Wang, et al., Ablation of ERO1A induces lethal endoplasmic reticulum stress responses and immunogenic cell death to activate anti-tumor immunity, Cell Rep. Med. (2023) 101206.
[15] J. Zhang, J. Yang, C. Lin, W. Liu, Y. Huo, M. Yang, et al., Endoplasmic Reticulum stress-dependent expression of ERO1L promotes aerobic glycolysis in Pancreatic cancer, Theranostics 10 (18) (2020) 8400–8414.
[16] A. Bassot, L. Violy, L. Gorka, L. Cigalotto, B. Namasivayam, I. Mikaelian, et al., ERO1a fosters glioblastoma aggressiveness and metabolic flexibility by regulating mitochondria-associated membrane dynamics, Nat. Cell Biol. (2026).
[17] T. Tanaka, T. Kajiwara, T. Torigoe, Y. Okamoto, N. Sato, Y. Tamura, Cancer-associated oxidoreductase ERO1-alpha drives the production of tumor-promoting myeloid-derived suppressor cells via oxidative protein folding, J. Immunol. 194 (4) (2015) 2004–2010.
[18] Y. Zhang, T. Li, L. Zhang, F. Shangguan, G. Shi, X. Wu, et al., Targeting the functional interplay between endoplasmic reticulum oxidoreductin-1alpha and protein disulfide isomerase suppresses the progression of cervical cancer, EBioMedicine 41 (2019) 408–419.
[19] E. Varone, A. Decio, A. Chernorudskiy, L. Minoli, L. Brunelli, F. Ioli, et al., The ER stress response mediator ERO1 triggers cancer metastasis by favoring the angiogenic switch in hypoxic conditions, Oncogene 40 (2021) 1721–1736.
[20] D. May, A. Itin, O. Gal, H. Kalinski, E. Feinstein, E. Keshet, Ero1-L alpha plays a key role in a HIF-1-mediated pathway to improve disulfide bond formation and VEGF secretion under hypoxia: implication for cancer, Oncogene 24 (6) (2005) 1011–1020.
[21] F. Zilli, P. Marques Ramos, P. Auf der Maur, C. Jehanno, A. Sethi, M.M. Coissieux, et al., The NFIB-ERO1A axis promotes breast cancer metastatic colonization of disseminated tumour cells, EMBO Mol. Med. (2021) e13162.
[22] T. Tanaka, G. Kutomi, T. Kajiwara, K. Kukita, V. Kochin, T. Kanaseki, et al., Cancer-associated oxidoreductase ERO1-alpha drives the production of VEGF via oxidative protein folding and regulating the mRNA level, Br. J. Cancer 114 (11) (2016) 1227–1234.
[23] T. Voron, O. Colussi, E. Marcheteau, S. Pernot, M. Nizard, A.L. Pointet, et al., VEGF-A modulates expression of inhibitory checkpoints on CD8+ T cells in tumors, J. Exp. Med. 212 (2) (2015) 139–148.
[24] E. Varone, A. Chernorudskiy, A. Cherubini, A. Cattaneo, A. Bachi, S. Fumagalli, et al., ERO1 alpha deficiency impairs angiogenesis by increasing N-glycosylation of a proangiogenic VEGFA, Redox Biol. 56 (2022) 102455.
[25] N.A. Cherepanova, S. Shrimal, R. Gilmore, Oxidoreductase activity is necessary for N-glycosylation of cysteine-proximal acceptor sites in glycoproteins, J. Cell Biol. 206 (4) (2014) 525–539.
[26] M. van Lith, M.A. Pringle, B. Fleming, G. Gaeta, J. Im, R. Gilmore, N.J. Bulleid, A cytosolic reductase pathway is required for efficient N-glycosylation of an STT3B-dependent acceptor site, J. Cell Sci. 134 (22) (2021).
[27] S.R. Stowell, T. Ju, R.D. Cummings, Protein glycosylation in cancer, Annu. Rev. Pathol. 10 (2015) 473–510.
[28] K. Asleh, G.L. Negri, S.E. Spencer Miko, S. Colborne, C.S. Hughes, X.Q. Wang, et al., Proteomic analysis of archival breast cancer clinical specimens identifies biological subtypes with distinct survival outcomes, Nat. Commun. 13 (1) (2022) 896.
[29] E. Varone, M. Retini, A. Cherubini, A. Chernorudskiy, A. Marrazza, A. Guidarelli, et al., Small molecule-mediated inhibition of the oxidoreductase ERO1A restrains aggressive breast cancer by impairing VEGF and PD-L1 in the tumor microenvironment, Cell Death Dis. 16 (1) (2025) 105.
[30] A. Le Naour, A. Rossary, M.P. Vasson, EO771, is it a well-characterized cell line for mouse mammary cancer model? Limit and uncertainty, Cancer Med. 9 (21) (2020) 8074–8085.
[31] J. Rappsilber, Y. Ishihama, M. Mann, Stop and go extraction tips for matrix-assisted laser desorption/ionization, nanoelectrospray, and LC/MS sample pretreatment in proteomics, Anal. Chem. 75 (3) (2003) 663–670.
[32] S. Tyanova, T. Temu, P. Sinitcyn, A. Carlson, M.Y. Hein, T. Geiger, et al., The Perseus computational platform for comprehensive analysis of (prote)omics data, Nat. Methods 13 (9) (2016) 731–740.
[33] Z. Xie, A. Bailey, M.V. Kuleshov, D.J.B. Clarke, J.E. Evangelista, S.L. Jenkins, et al., Gene set knowledge discovery with Enrichr, Curr. Protoc. 1 (3) (2021) e90.
[34] S. Germani, A.T. Van Ho, A. Cherubini, E. Varone, A. Chernorudskiy, G.M. Renna, et al., SEPN1-related myopathy depends on the oxidoreductase ERO1A and is druggable with the chemical chaperone TUDCA, Cell Rep. Med. (2024) 101439.
[35] E. Zito, H.G. Hansen, G.S. Yeo, J. Fujii, D. Ron, Endoplasmic reticulum thiol oxidase deficiency leads to ascorbic acid depletion and noncanonical scurvy in mice, Mol. Cell 48 (2012) 39–51.

[36] P. Workman, E.O. Aboagye, F. Balkwill, A. Balmain, G. Bruder, D.J. Chaplin, et al., Guidelines for the welfare and use of animals in cancer research, Br. J. Cancer 102 (11) (2010) 1555–1577.
[37] C. Imbert, A. Montfort, M. Fraisse, E. Marcheteau, J. Gilhodes, E. Martin, et al., Resistance of melanoma to immune checkpoint inhibitors is overcome by targeting the sphingosine kinase-1, Nat. Commun. 11 (1) (2020) 437.
[38] M. Retini, A. Cherubini, A. Marrazza, E. Varone, S. Germani, G.M. Renna, et al., Pyrazolone-based ERO1 inhibitors in ERO1-driven triple-negative breast cancer and SEPN1-Related myopathy: structure-activity relationship and therapeutic potential, Pharmacol. Res. (2025) 108037.
[39] Y. Hao, T. Stuart, M.H. Kowalski, S. Choudhary, P. Hoffman, A. Hartman, et al., Dictionary learning for integrative, multimodal and scalable single-cell analysis, Nat. Biotechnol. 42 (2) (2024) 293–304.
[40] P.L. Germain, A. Lun, C. Garcia Meixide, W. Macnair, M.D. Robinson, Doublet identification in single-cell sequencing data using scDblFinder, F1000Res 10 (2021) 979.
[41] I. Korsunsky, N. Millard, J. Fan, K. Slowikowski, F. Zhang, K. Wei, et al., Fast, sensitive and accurate integration of single-cell data with Harmony, Nat. Methods 16 (12) (2019) 1289–1296.
[42] T.S. Heng, M.W. Painter, Immunological genome project C. The immunological genome project: networks of gene expression in immune cells, Nat. Immunol. 9 (10) (2008) 1091–1094.
[43] S.S. Pinho, C.A. Reis, Glycosylation in cancer: mechanisms and clinical implications, Nat. Rev. Cancer 15 (9) (2015) 540–555.
[44] M. Koritzinsky, F. Levitin, T. van den Beucken, R.A. Rumantir, N.J. Harding, K. C. Chu, et al., Two phases of disulfide bond formation have differing requirements for oxygen, J. Cell Biol. 203 (4) (2013) 615–627.
[45] C.W. Li, S.O. Lim, W. Xia, H.H. Lee, L.C. Chan, C.W. Kuo, et al., Glycosylation and stabilization of programmed death ligand-1 suppresses T-cell activity, Nat. Commun. 7 (2016) 12632.
[46] T. Tanaka, G. Kutomi, T. Kajiwara, K. Kukita, V. Kochin, T. Kanaseki, et al., Cancer-associated oxidoreductase ERO1-alpha promotes immune escape through up-regulation of PD-L1 in human breast cancer, Oncotarget 8 (15) (2017) 24706–24718.
[47] D. Lau, A.M. Bobe, A.A. Khan, RNA sequencing of the tumor microenvironment in precision cancer immunotherapy, Trends Cancer 5 (3) (2019) 149–156.
[48] P. Walter, D. Ron, The unfolded protein response: from stress pathway to homeostatic regulation, Science 334 (6059) (2011) 1081–1086.
[49] N. Rufo, A.D. Garg, P. Agostinis, The unfolded protein response in immunogenic cell death and cancer immunotherapy, Trends Cancer 3 (9) (2017) 643–658.
[50] C.H. Tang, S. Ranatunga, C.L. Kriss, C.L. Cubitt, J. Tao, J.A. Pinilla-Ibarz, et al., Inhibition of ER stress-associated IRE-1/XBP-1 pathway reduces leukemic cell survival, J. Clin. Investig. 124 (6) (2014) 2585–2598.
[51] S. Lhomond, T. Avril, N. Dejeans, K. Voutetakis, D. Doultsinos, M. McMahon, et al., Dual IRE1 RNase functions dictate glioblastoma development, EMBO Mol. Med. 10 (3) (2018).
[52] Z. Yang, Y. Huo, S. Zhou, J. Guo, X. Ma, T. Li, et al., Cancer cell-intrinsic XBP1 drives immunosuppressive reprogramming of intratumoral myeloid cells by promoting cholesterol production, Cell Metab. 34 (12) (2022) 2018–20135 e8.
[53] J.R. Cubillos-Ruiz, P.C. Silberman, M.R. Rutkowski, S. Chopra, A. Perales-Puchalt, M. Song, et al., ER stress sensor XBP1 controls anti-tumor immunity by disrupting dendritic cell homeostasis, Cell 161 (7) (2015) 1527–1538.
[54] M. Song, T.A. Sandoval, C.S. Chae, S. Chopra, C. Tan, M.R. Rutkowski, et al., IRE1alpha-XBP1 controls T cell function in ovarian cancer by regulating mitochondrial activity, Nature 562 (7727) (2018) 423–428.
[55] K. DePeaux, G.M. Delgoffe, Metabolic barriers to cancer immunotherapy, Nat. Rev. Immunol. 21 (12) (2021) 785–797.
[56] X. Chen, J.R. Cubillos-Ruiz, Endoplasmic reticulum stress signals in the tumour and its microenvironment, Nat. Rev. Cancer 21 (2) (2021) 71–88.
[57] B. Virassamy, F. Caramia, P. Savas, S. Sant, J. Wang, S.N. Christo, et al., Intratumoral CD8(+) T cells with a tissue-resident memory phenotype mediate local immunity and immune checkpoint responses in breast cancer, Cancer Cell (2023).
[58] E. Varone, A. Decio, M.C. Barbera, M. Bolis, L. Di Rito, F. Pisati, et al., Endoplasmic reticulum oxidoreductin 1-alpha deficiency and activation of protein translation synergistically impair breast tumour resilience, Br. J. Pharmacol. 179 (23) (2022) 5180–5195.
[59] C. Zhong, P. Li, S. Argade, L. Liu, A. Chilla, W. Liang, et al., Inhibition of protein glycosylation is a novel pro-angiogenic strategy that acts via activation of stress pathways, Nat. Commun. 11 (1) (2020) 6330.
[60] J. Yang, C. Wang, D. Fu, L.L. Ho, K. Galani, L. Chen, et al., Mature and migratory dendritic cells promote immune infiltration and response to anti-PD-1 checkpoint blockade in metastatic melanoma, Nat. Commun. 16 (1) (2025) 8151.
[61] J.D. Blais, K.T. Chin, E. Zito, Y. Zhang, N. Heldman, H.P. Harding, et al., A small molecule inhibitor of endoplasmic reticulum oxidation 1 (ERO1) with selectively reversible thiol reactivity, J. Biol. Chem. 285 (27) (2010) 20993–21003.
[62] T. Castrignano, S. Gioiosa, T. Flati, M. Cestari, E. Picardi, M. Chiara, et al., ELIXIR-IT HPC@CINECA: high performance computing resources for the bioinformatics community, BMC Bioinf. 21 (Suppl 10) (2020) 352.
[63] A. Athar, A. Fullgrabe, N. George, H. Iqbal, L. Huerta, A. Ali, et al., ArrayExpress update - from bulk to single-cell expression data, Nucleic Acids Res. 47 (D1) (2019) D711–D715.
[64] Y. Perez-Riverol, C. Bandla, D.J. Kundu, S. Kamatchinathan, J. Bai, S. Hewapathirana, et al., The PRIDE database at 20 years: 2025 update, Nucleic Acids Res. 53 (D1) (2025) D543–D553.